The Journal of Chemical Physics

Transient superdiffusion of polydisperse vacuoles in highly motile amoeboid cells

Cite as: J. Chem. Phys. **150**, 144901 (2019); https://doi.org/10.1063/1.5086269
Submitted: 19 December 2018 . Accepted: 03 March 2019 . Published Online: 09 April 2019

Samudrajit Thapa, Nils Lukat, Christine Selhuber-Unkel, Andrey G. Cherstvy, and Ralf Metzler

The Journal of Chemical Physics ARTICLE scitation.org/journal/jcp

Transient superdiffusion of polydisperse vacuoles in highly motile amoeboid cells

Cite as: J. Chem. Phys. 150, 144901 (2019); doi: 10.1063/1.5086269
Submitted: 19 December 2018 • Accepted: 3 March 2019 •
Published Online: 9 April 2019

Samudrajit Thapa,[1] Nils Lukat,[2] Christine Selhuber-Unkel,[2,a)] Andrey G. Cherstvy,[1] and Ralf Metzler[1,b)]

AFFILIATIONS

[1]Institute for Physics and Astronomy, University of Potsdam, 14476 Potsdam-Golm, Germany
[2]Institute of Materials Science, Christian-Albrechts-Universität zu Kiel, 24143 Kiel, Germany

Note: This article is part of the Special Topic "Chemical Physics of Active Matter" in J. Chem. Phys.
[a)]**Electronic mail:** cse@tf.uni-kiel.de
[b)]**Electronic mail:** rmetzler@uni-potsdam.de

ABSTRACT

We perform a detailed statistical analysis of diffusive trajectories of membrane-enclosed vesicles (vacuoles) in the supercrowded cytoplasm of living *Acanthamoeba castellanii* cells. From the vacuole traces recorded in the center-of-area frame of moving amoebae, we examine the statistics of the time-averaged mean-squared displacements of vacuoles, their generalized diffusion coefficients and anomalous scaling exponents, the ergodicity breaking parameter, the non-Gaussian features of displacement distributions of vacuoles, the displacement autocorrelation function, as well as the distributions of speeds and positions of vacuoles inside the amoeba cells. Our findings deliver novel insights into the internal dynamics of cellular structures in these infectious pathogens.

I. INTRODUCTION

Free-living protozoa *Acanthamoeba castellanii* (abbreviated AC below) form a family of pathogens causing life-threatening infections in humans (including blinding keratitis, fatal encephalitis, and meningoencephalitis).[1–4] These amoeboid parasites are abundant in water-, air-, and soil-containing environments, including lakes, swimming pools, beaches, and are also present in tap and bottled water.[1,4] AC cells also use air-conditioning and dental-treatment units as their habitats. They are a threat at hospitals, also affecting the eyes of users of contact lenses and attacking lung tissues.[3] AC trophozoite cells range ≈12–30 μm in diameter, adapting ellipsoidal shapes.[3,5,6] These amoebae feature ~μm-long spiky flat acanthopodia structures on their surfaces.[5,7] AC cells feed on microorganisms via phagocytosis (invagination by membrane vesicles).

The cytoplasm of AC cells is a supercrowded viscoelastic environment[8] with crowders varying in nature and size (large biopolymers, granules, and vacuoles). This fact poses serious challenges for the motion and function of cell organelles and active transport inside these amoebae. A better understanding of the basic physico-chemical mechanisms of motion of various cellular components and organelles in the AC cytoplasm is crucial to unravel the functional principles and virulent properties of these amoeboid pathogens.

Internal vacuoles are highly abundant in the AC cytoplasm, and they range from submicrons to several μm in radius (Fig. 1). The vacuoles play crucial roles in the AC life-cycle and metabolism.[5] Some vacuoles are employed to internalize and incapacitate potentially threatening foreign particles and as reservoirs for materials, while others are used for food storage and digestion. A water-expulsion vesicle (or contractile vacuole[9]) regulates the osmotic conditions inside these protozoan cells.[7,10] We refer to Refs. 1 and 3–5 for further details on the life cycle as well as on feeding, survival, reproduction, and host-infection pathways of AC cells.

Similar to other self-propelled, crawling amoebae (such as *Dictyostelium discoideum*[11,12]), the locomotion of AC cells is due to formation of actin-based protrusions[13–16] on their leading edge. The motion of amoeboid cells can be studied by a number of single-particle tracking (SPT) techniques.[17] Physically, crawling cells often employ actin treadmilling in the front and myosin-induced contraction on the back of the cell to maintain propulsion.[16] The protrusions are often established by actin treadmilling, supporting the growth of a lamellipodium forming the leading edge in the

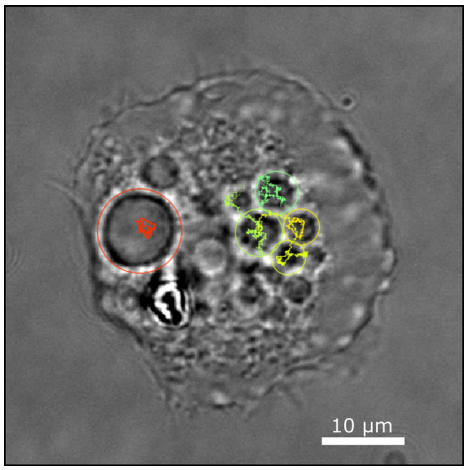

FIG. 1. Experimental image of vacuoles inside an AC cell on a solid substrate. Several vacuole trajectories after tracking for 1290 s are shown.

direction of motion. Certain values of cell–substrate adhesion[16,18–20] and traction strengths[14,15,21] as well as of the interfacial membrane tensions are required for this locomotion. A minimal model of cell motility based on a droplet of active actomyosin fluid was developed in Ref. 16.

The diffusive properties of endogenous intracellular particles of varying sizes in the cytoplasm of AC cells were examined recently;[8] see also Ref. 22. The cytoskeletal elements (microtubuli and actin) serve as tracks for intrinsically processive motor proteins (kinesin/dynein and myosin, respectively); see Refs. 6, 8, 9, and 23–29. These motors actively carry intracellular particles as cargos and ensure precise transport and swift exchange of materials inside cells of multiple types. Therefore, potentially active transport of AC vacuoles can lead to superdiffusion, as detected (at least transiently).[8,22] In AC cells, the microtubuli often radiate from their one-end focus located near the Golgi complex; see, e.g., Refs. 5 and 6.

The superdiffusive motion of vacuoles may involve motor proteins attached to them. For instance, dynein and kinesin proteins walk on microtubuli toward the cell center and its periphery[25,31–33] (performing, respectively, minus-end- and plus-end-directed motions along microtubuli). This ensures a directional transport of cargos—various organelles, membrane-bound vesicles,[33] and other reactants (protein complexes, mRNA, etc.)—through the cytoplasm. Nevertheless, after treatment of AC cells with nocodazole and latrunculin A—specific drugs inhibiting the polymerization process of actin and microtubuli, respectively,[16,30] and thereby hampering AC propulsion—the vacuoles can still move superdiffusively.[8] By contrast, when the activity of myosin-II motors is inhibited by blebbistatin, the vacuoles are almost stalled for a prolonged period of time.[8,119] In addition, amoeba locomotion *per se* may contribute to superdiffusion of its internal vacuoles (in the center-of-area frame of each cell).[8]

Despite recent scientific progress for a number of other locomotive cell systems—in particular, from advanced SPT-measurements and data-analysis tools—the exact physical mechanisms of both driven and passive diffusion of intracellular organelles and artificial tracers inside moving AC cells are still not fully understood. Therefore, the statistical quantification of vacuole motion—as well as of vacuole granules involved in the pathogenicity of these amoebae—is the main focus of the current study. The new sights found here for the detailed transport behavior will be an important ingredient for establishing a more complete physical and biochemical picture of AC motility and its underlying mechanisms.

The paper is organized as follows. We start with the description of the data-acquisition protocol in Sec. II. In Sec. III, we define all observables and diffusion measures for the main text. The results of the data analysis are presented in Sec. IV. Specifically, we consider the distributions of vacuole sizes and trajectory lengths in Sec. IV A, the spread of their time-averaged mean-squared displacements (TAMSDs) in Sec. IV B, the correlation of diffusion coefficients and scaling exponents for each trajectory in Sec. IV C, the ergodicity breaking (EB) parameter in Sec. IV D, and the distribution of vacuole displacements in Sec. IV E. The displacement autocorrelation function is described in Sec. IV F, and the distribution of instantaneous speeds and positions of vacuoles is presented in Sec. IV G. In Sec. V A, we summarize the main results. Finally, in Sec. V C, we overview some related systems and discuss possible mathematical models applicable to the examined data. In Sec. V C, we finish with mentioning future research directions. Additional figures are presented in the Appendix.

II. EXPERIMENTAL CONDITIONS AND DATA ACQUISITION STRATEGY

AC cells were cultured at room temperature following the protocol of Ref. 8. For imaging purposes, amoeboid cells at low concentration were seeded on a glass well (ibidi 60 μ-dish, 35-mm high, glass bottom). The imaging procedure was conducted using a Hamamatsu ORCA ER 2 camera on an Olympus IX 71 microscope using 60× magnification (Olympus UPLANSAPO 60×/1.35 NA oil-immersion objective) in the phase-contrast mode. The AC cells adhere to the substrate, but their 3D shape is different from that of mammalian adhesive cells. Whereas in differential interference contrast microscopy the dome-like shape of mammalian cells, such as fibroblasts, is clearly visible (see, e.g., Ref. 34), *Acanthamoeba* trophozoites often have an ellipsoidal shape and do not strongly flatten in height toward the edges.[35] In the surface-adhered state, our AC cells are rather "Lebkuchen"-like in shape.

The images were recorded with the Image Acquisition Toolbox in `Matlab` (Mathworks, Inc.) with recording frequency ≈8.95 fps (step time $dt \approx 0.11$ s). Every two seconds, the images were segmented using an edge-detection algorithm (`Matlab`) and the centers-of-area of AC cells were evaluated. To ensure long-time SPT recordings, the center of the image was adjusted to the center-of-area of a given cell via automatically moving along a scanning stage (Märzhäuser, SCAN IM 112 × 74). While post-processing the acquired videos, the center-of-area of each amoeba was evaluated and static-motion videos were produced. Static-motion videos were used for the edge-detection algorithm, and the Hough transformation was used to define the geometric circles of vacuoles and respective positions of their centers. The location of intracellular vacuoles at each step was enumerated in the center-of-area

frame of the cell using the new in-house segmentation algorithm (Matlab).

The video files reveal bright circles surrounding the vacuoles. First, the edge-detection algorithm was used to find the edges of frames of the static-motion videos. To detect the positions of vacuole "circles," in the binary-image file, a Hough transformation was implemented. To refine the obtained position, a region of pixels around a possible center position was set. To compute the radius of the bright circle (vacuole), the mean intensity of pixels at each radial distance from each pixel in the preselected area was calculated; see the scheme in Fig. 11 in the Appendix. This procedure was repeated for all possible radii, from a minimal to a maximal one. The refined position of the vacuole center was then chosen as the pixel in the image which yields the highest intensity value. The respective radius was set as the vacuole radius; at each time step, the center positions and radii of all the vacuoles were stored in the data set; see Fig. 12 in the Appendix. Manual confirmation of the detected vacuoles was obtained by saving the data into an xml-file readable in Matlab with the help of MaMut and ImageJ plug-ins.

Experimental SPT tracks of vacuoles were analyzed using the @msdanalyzer procedure (Matlab); see Refs. 22, 36, and 37. Vacuole trajectories shorter than $T_{\min} \approx 60$ frames were discarded from the analysis, and the maximal trace length was $T_{\max} \approx 27\,700$ frames. Automatically determined trajectories were controlled manually for consistency and continuity. Adjusting the center positions of vacuoles, we define their time-local radii (at a point of highest intensity).[120] The video files of tracked vacuoles—speed up 100× as well as in real time—can be found in the supplementary material [each video has a counter in the corner (h:min:s)]. They show the formation of protrusions on the leading edge of the AC cells. For amoebae cells #1, 2, 3, and 4, we record $N_1 = 144$, $N_2 = 18$, $N_3 = 14$, and $N_4 = 205$ vacuole trajectories, respectively. The center of the view-field and the center-of-area of amoebae superimpose in the image and in video files.

The uncertainty in determining the amoeba and vacuole positions is a couple of pixels of the microscopy image, with 1 pixel ≈ 0.106 μm. The tracked AC cells are often ellipsoids but display large shape variations. In moving AC cells, the vacuoles are observed in the SPT experiments in almost one horizontal plane. Therefore, the SPT experiments of vacuole motion effectively take place in two dimensions.[8] The center of a vacuole is assigned to the center of a pixel, and vacuole motion is recorded in multiples of the pixel width. We observe that some (especially small) vacuoles disappear from the view-field in the focal plane (i.e., because of vacuole overlap). The diffusive properties of vacuoles are examined in the center-of-area frame of respective AC cells.[121]

III. DIFFUSIVE CHARACTERISTICS AND PHYSICAL OBSERVABLES

For standard Brownian motion, the ensemble-averaged mean-squared displacement (MSD) of diffusing particles grows linearly with time, also called Fickian diffusion. For stochastic processes featuring anomalous diffusion, the MSD grows nonlinearly with time. Namely, in two dimensions (relevant for the current SPT scenario), one has[38–45]

$$\left\langle [x(t) - x(0)]^2 + [y(t) - y(0)]^2 \right\rangle = 4K_\alpha t^\alpha \simeq t^\alpha. \tag{1}$$

Here, α is the anomalous scaling exponent, K_α is the generalized diffusion coefficient, and the angular brackets denote ensemble averaging. For subdiffusive processes the exponent is in the range $0 < \alpha < 1$, while for superdiffusion one has $\alpha > 1$. Anomalous diffusion is ubiquitous in cell-related contexts (both sub-[40,42,44–54] and superdiffusion[8,12,29,55–57]) and artificially crowded media.

The standard SPT observable is the TAMSD, defined for the ith vacuole (in the continuous representation) as[38,39,43,44]

$$\overline{\delta_i^2(\Delta)} = \frac{1}{T-\Delta}\int_0^{T-\Delta} \left\{ [x_i(t+\Delta) - x_i(t)]^2 + [y_i(t+\Delta) - y_i(t)]^2 \right\} dt. \tag{2}$$

The analog of Eq. (2) for time series at discrete times is straightforward. The mean over N independent trajectories each with length T_i is computed as

$$\left\langle \overline{\delta^2(\Delta)} \right\rangle = N^{-1} \sum_{i=1}^{N} \overline{\delta_i^2(\Delta)}, \tag{3}$$

where $0 \le \Delta \le T_i$ is the lag time involved in averaging of the recorded time series $\{x_i(t), y_i(t)\}$. For SPT trajectories of different lengths, at different lag times the respective number $N(\Delta)$ in Eq. (3) changes as well. At short lag times, we fit the individual TAMSDs by two-parameter power-laws

$$\overline{\delta_i^2(\Delta)} \approx 4 \times (K_\beta)_i \times \Delta^{\beta_i}. \tag{4}$$

Here, $(K_\beta)_i$ is the trajectory-specific generalized diffusion coefficient for the TAMSD $\overline{\delta_i^2(\Delta)}$. A fairly small number of experimental SPT frames are used below for this fit: $n_{\rm fit}$ is from 5 to 25 points along the trajectories (independent of their total length). One point is equivalent to one frame in the SPT experiment. Statistically, the TAMSD delivers the most reliable results for short lag times, when $\Delta/T \ll 1$.[37,43] We refer here to Refs. 58 and 59 for the analysis of some effects of $n_{\rm fit}$ and of uncertainties of the particle-localization procedure on the values of β_i and $(K_\beta)_i$ (see also Refs. 12 and 37).

To quantify the spread of $\overline{\delta_i^2(\Delta)}$ for an ensemble of vacuoles, after a given lag time Δ we compute the ergodicity breaking parameter as the ensemble average[38–40,43,60]

$$\mathrm{EB}(\Delta) = \left\langle \left(\overline{\delta^2(\Delta)} \right)^2 \right\rangle \Big/ \left\langle \overline{\delta^2(\Delta)} \right\rangle^2 - 1. \tag{5}$$

For Brownian motion, the EB parameter scales in the region $\Delta/T \ll 1$ as[43,60–63]

$$\mathrm{EB}_{\rm BM}(\Delta) \approx 4\Delta/(3T), \tag{6}$$

while other functional forms of EB(Δ) are known, especially finite EB values even at long measurement times.[38,43,64]

We also compute the displacement autocorrelation function $C_{\delta t}(t)$ from the two-dimensional radius-vector of vacuoles, $\mathbf{r}_i(t)$, as

$$C_{\delta t}(t) = (\delta t)^{-2} \times \langle [\mathbf{r}_i(t+\delta t) - \mathbf{r}_i(t)] \cdot [\mathbf{r}_i(\delta t) - \mathbf{r}_i(0)] \rangle. \tag{7}$$

This function quantifies displacement correlations along the trajectories after a finite time shift δt; see Refs. 39, 43, 44, and 65. Instantaneous speeds of vacuoles and their radial distributions in the course of intracellular diffusion are also evaluated.

IV. MAIN RESULTS

A. Distribution of vacuole sizes and trajectory lengths

The radii of the tracked vacuoles are rather broadly distributed, from ≈1 to ≈4.5 μm, as shown in Fig. 2. The SPT data for a total of $N = 357$ vacuole trajectories are analyzed (for most of the results below). The statistical and fitting analysis is performed in `Matlab` and `Wolfram Mathematica`. Certain vacuoles are quite dynamic entities, capable of changing their (visible and real) dimensions on time scales from several seconds to dozens of minutes.[10] For the current data set, the largest vacuole is often observed to grow in size and then abruptly shrink (see the supplementary video files). This cycle repeats as the amoeba moves, see the radius evolution in Fig. 13(a) in the Appendix, indicating that this vacuole is the contractile vacuole expelling water for osmotic regulation.[5,66]

For small and medium-sized vacuoles, the radius variations in the SPT data files are considerably smaller [Fig. 13(b) in the Appendix]. Moreover, as the vacuoles move across the focal plane, their *effective radii* can change along the recorded time series. This is particularly pronounced for small vacuoles, for which insignificant displacements perpendicular to the focal plane can give rise to large relative variations of their visible size. Therefore, in Fig. 2 we compute and analyze the *maximal* radii along the recorded time series, which reflects the physical vacuole sizes quite closely. However, the analysis using the *mean* vacuole radius illustrated in Fig. 13(b) in the Appendix—for instance, to study the distribution of vacuoles in cells as quantified in Fig. 21 in the Appendix—can also be a legitimate procedure.

B. TAMSD: Magnitudes, spread of trajectories, and anomalous scaling exponents

The distribution of trajectory lengths of small, medium, and large vacuoles is shown in Fig. 14 in the Appendix. We find that the subpopulation of the smallest vacuoles in the set features the shortest trajectories, medium-sized particles have intermediate-to-long traces, while the largest vacuoles yield longest time series. This observation is consistent with the physical mechanism that smaller vacuoles are quicker to leave the focal plane of the microscope via diffusion.[122] As mentioned in Ref. 8, the centers-of-area of AC cells perform nearly ballistic motion, with the scaling exponent

$$\langle \beta_{\mathrm{AC}} \rangle = 1.86 \pm 0.02 \tag{8}$$

of the mean TAMSD $\left\langle \overline{\delta^2(\Delta)} \right\rangle$; see Fig. 15 in the Appendix. From these data, the average "speed" of AC cells for the current conditions (temperature, surface adhesion, etc.) can be estimated as $\langle v_{\mathrm{AC}} \rangle \approx 0.49\ \mu$m/s.

Dividing up the vacuoles by their sizes, as color-coded in Fig. 2, Fig. 3 presents the individual TAMSDs of the tracked particles for the respective subpopulations. We find that small, medium, and large vacuoles yield mean TAMSDs of similar magnitude and functional dependence; see the thick solid curves in Fig. 3.

We find that the TAMSDs are slightly subdiffusive at very short lag times,[69] progressively turning superdiffusive at intermediate Δ and, finally, exhibiting subdiffusion again at even longer times. Different AC cells reveal a close match of the MSD and mean TAMSD evolution at short-to-intermediate times; see Fig. 16 in the Appendix. From the data of Fig. 3 for lag times up to 20 s, the average diffusion coefficient of vacuoles is $D_{\mathrm{vac}} \approx 0.09\ \mu\mathrm{m}^2/\mathrm{s}$. For comparison, the Stokes-Einstein diffusivity of a spherical particle with radius 3 μm in water is ≈0.1 $\mu\mathrm{m}^2/\mathrm{s}$. As an alternative to the average diffusivity, D_{vac}, the frame-based[70] and time-local[71] diffusion coefficients can also be used in the analysis.

The time-local anomalous scaling exponent for the mean TAMSD of vacuoles is defined as[39,41–43]

$$\langle \beta(\Delta) \rangle = \partial \log\left(\left\langle \overline{\delta^2(\Delta)} \right\rangle \right) / \partial \log \Delta. \tag{9}$$

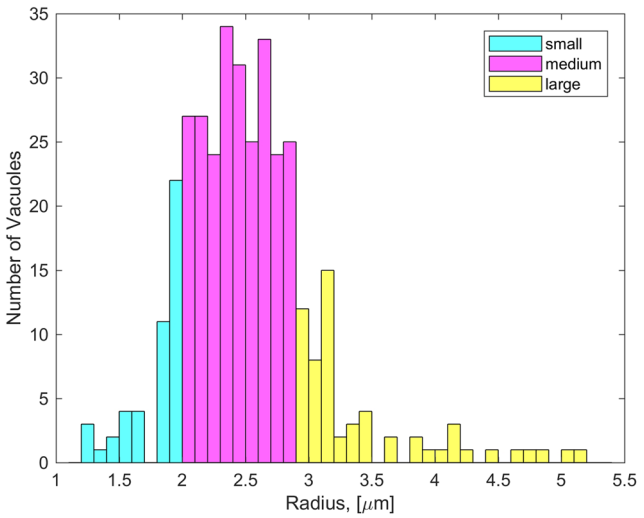

FIG. 2. Distribution of radii of vacuoles diffusing in the AC cytoplasm. The subpopulations were chosen to quantify the ≈13% smallest, ≈70% medium-sized, and ≈17% largest vacuoles.

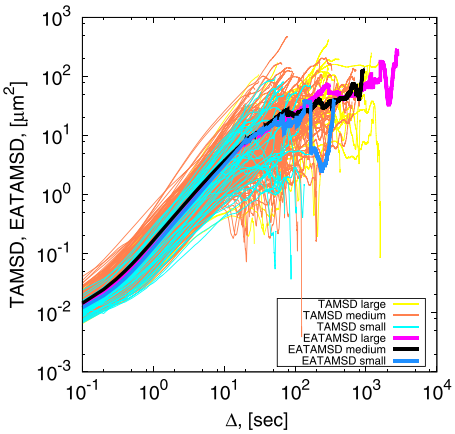

FIG. 3. Spread of individual TAMSDs (2) of vacuoles. Different colors denote different subpopulations of vacuoles (see Fig. 2). The mean TAMSDs (3) for each subpopulation are represented by the thick solid lines. For longer lag times the statistics becomes poorer, as expected.

Its variation with the lag time is illustrated in Fig. 4. The transition from short-lag-time subdiffusion to intermediate-time superdiffusion and back to subdiffusion is particularly visible for a smaller number of points ($n_{\rm fit}$) used in the fit analysis of Eqs. (4) and (9). The most superdiffusive behavior with

$$\langle \beta_{\rm vac} \rangle \approx 1.2\text{–}1.4 \tag{10}$$

is observed at lag times $\Delta \approx 1$–5 s; see Fig. 4 and also the analysis of Ref. 22. Large variations in $\langle \beta(\Delta) \rangle$ at $\Delta \gg 5$–10 s are caused by insufficient statistics in the averaging procedure (2). Note that for varying $n_{\rm fit}$ values the $\langle \beta_{\rm vac}(\Delta) \rangle$ curves are plotted in Fig. 4 starting from the lag time $\delta\Delta \times n_{\rm fit}/2$ (the middle of the respective fitting interval). As physically expected, as the number of fitting points increases, the variations of the resulting scaling exponent with lag time decrease because the fit is done over larger intervals of the TAMSDs. For the effects of $n_{\rm fit}$ on the value of short-time diffusivity, including a choice of an optimal $n_{\rm fit}$ value, we refer to Refs. 58, 59, 65, and 72.

C. K_β–β correlations and $p(K_\beta)$ distribution

Our analysis reveals positive correlations between the values of the generalized diffusion coefficient and the anomalous scaling exponent of the TAMSDs computed for individual vacuoles at short lag times. Figure 5 shows these results for the minimal lag-time value, $\Delta = 0.1$ s. We fit these correlations with an exponential function

$$K_\beta(\beta_{\rm vac}) \sim \exp[c_1 \beta_{\rm vac} + c_2], \tag{11}$$

where $c_{1,2}$ are fit coefficients. The correlations are somewhat stronger for smallest numbers of fitting points in Eq. (4); see Fig. 5. This trend is similar to that observed for free Brownian motion as well as for confined diffusion obeying the Ornstein-Uhlenbeck process, as we checked by computer simulations; see Fig. 18 in the Appendix. These positive correlations at short lag times indicate that the motion of vacuoles in AC cells with *larger* exponents features *larger* diffusion coefficients.

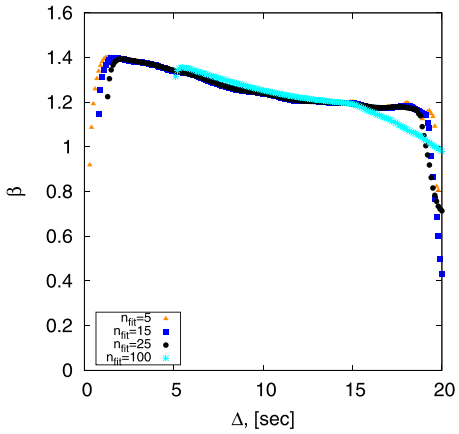

FIG. 4. Time-local anomalous diffusion exponent of the mean TAMSD of vacuoles (computed for vacuoles of all sizes in Fig. 2), plotted versus the lag time for varying number of points ($n_{\rm fit}$) in the fit of Eq. (4).

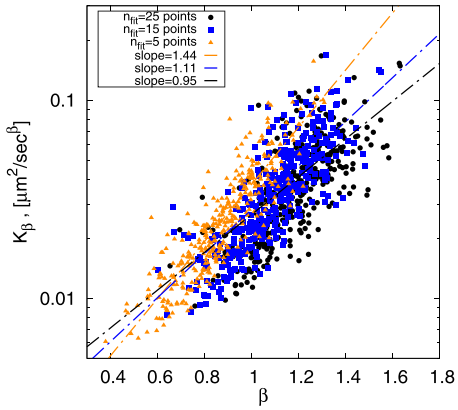

FIG. 5. Correlations of anomalous scaling exponents and generalized diffusion coefficients as obtained from the fit of individual TAMSDs (4) for vacuole motion. The initial lag time is $\Delta_{\rm start} = 0.1$ s. The dashed lines are the best linear fits to the data [in log-linear scale, see Eq. (11)]. The slope values in the legend here and below are linked to Eq. (11) as c_1 = slope × $\log_e$ 10.

The same analysis performed at later parts of the vacuole trajectories—starting, for instance, at $\Delta_{\rm start} = 1$ s as shown in Fig. 17(a) in the Appendix—reveals almost no remaining K_β–β correlations in the data. We refer here also to the analysis of *negative* K_β–β correlations for another amoeboid system[12] as well as to the recent study of spreading of nanoparticles and quantum dots in live mammalian cells. For the latter system, various nontrivial K_β–β dependencies were observed.[56] For even longer lag times—at $\Delta_{\rm start} = 10$ s as in Fig. 17(b) in the Appendix—the correlations turn *pronouncedly negative*, with $c_1 < 0$ in Eq. (11). Physically, in this case a larger diffusivity for a given vacuole trajectory K_β gives rise to statistically favorable smaller values of the anomalous exponent β_i attributable to it, and visa versa. This transition from positive to negative K_β versus β correlations is—at least partly—due to a more confined motion of vacuoles at later lag times (see also Sec. V A).

We also quantify the distribution $p(K_\beta)$ of the observed generalized diffusion coefficients; see Fig. 19 in the Appendix. We find that $p(K_\beta)$ is a fast decaying distribution, for varying numbers $n_{\rm fit}$ used in the scaling analysis. We mention here that the distribution $p(K_\beta)$ was examined for some recent experimental STP-data[56,73] as well as for certain anomalous diffusion processes (see the analysis of *in silico* trajectories performed in Refs. 74 and 75).

D. Ergodicity breaking parameter

The evolution of the EB parameter computed via (5) for the data on vacuole diffusion is presented in Fig. 6. We find that almost in the entire range of lag times the EB values are *considerably larger* than those for Brownian motion [Eq. (6)]. For longer lag times—similar to the behavior of the TAMSDs in Fig. 3—the ergodicity breaking parameter reveals large fluctuations due to worsening statistics (outside of the range used in Fig. 6). Note also that in Fig. 6 we show the EB variation in the same domain of lag times as in Fig. 4.[123]

In the inset of Fig. 6, we show the behavior of the EB parameter at short lag times versus the trajectory length, T. The decay

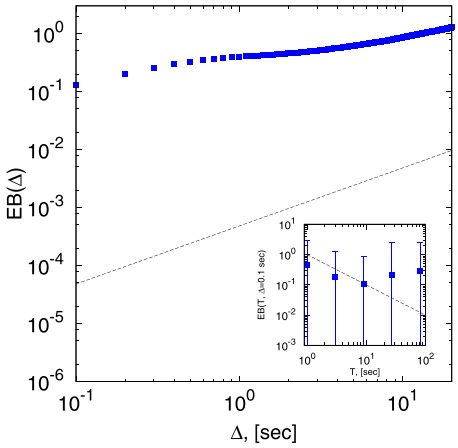

FIG. 6. Ergodicity breaking parameter (5) computed for all vacuole trajectories of Fig. 3 (with no separation in subpopulations). The inset shows the dependence of EB computed at $\Delta = 0.1$ s versus the trajectory length T for *partial* time series. The Brownian asymptote (6) is the dashed line.

appears to be slower than the inverse proportionality $1/T$, which is characteristic for a number of normal and anomalous diffusion processes.[39,43] The large magnitude of the standard error bars in Fig. 6 indicates, however, that the current sample is likely too small to make a solid statement regarding the EB(T) decay. As the standard deviation σ for a set of x_j values, defined as $\sigma(x) = \sqrt{N^{-1}\sum_{i=1}^{N}(x - \langle x \rangle)^2}$, decreases for a larger sample-size N, smaller error bars and more confident EB evaluation are expected when more SPT trajectories are available for the analysis (independent and taken at identical conditions).

E. Vacuole displacement distribution

The fine structure of the displacement distribution function $P(dr, dt)$ of vacuoles moving inside AC cells is visualized in Fig. 7. The radial displacement of vacuoles is computed as $dr = \sqrt{dx^2 + dy^2}$. We find that, particularly at short time shifts, $dt = 1$, the function $P(dr, dt)$ reveals three extremely pronounced peaks. They stem from discrete increments of vacuole positions in the data set which are often multiples of the pixel size, namely, $\{dx, dy\} \approx n \times 0.106\ \mu$m. Inherently, the observed behavior on the initial stages of vacuole diffusion is therefore far from a Gaussian; see Fig. 7(a). For longer time shifts, the distributions $P(dr, dt)$ also exhibit dramatic discreteness effects. For instance, again noting,[69] after ten steps, multiple peaks are clearly visible at $dx \approx n \times 0.1\ \mu$m in Fig. 7(b) [which can be smoothened if wider bins are used, as in the inset of Fig. 7(b)].

F. Autocorrelation function of displacements

The results for the displacement autocorrelation function computed for vacuole diffusion are shown in Fig. 8. Averaging is performed here over all particles, without division into subpopulations. We find that for short time shifts—for instance, at $\delta t = 1$ in Eq. (7)—the autocorrelation function drops below zero. Its negative values are consistent with subdiffusive motion observed for the TAMSDs at very short lag times; see Fig. 4. Remembering possible limitations of the experimental setup,[69] this antipersistence of

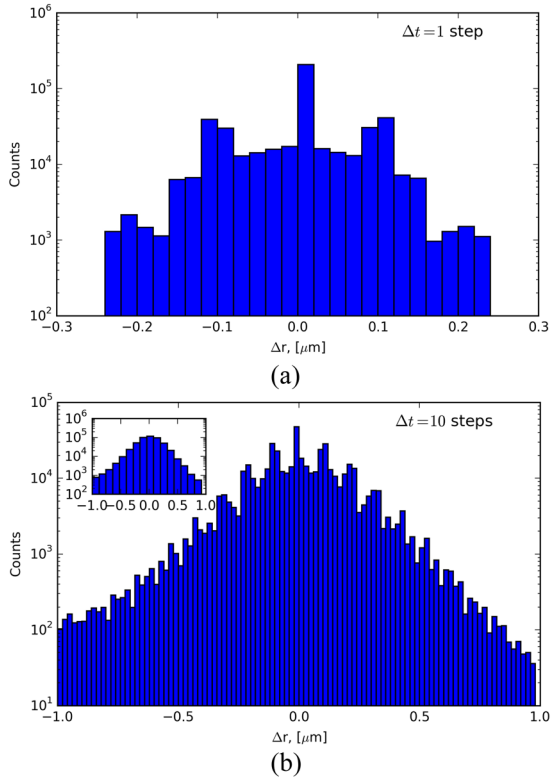

FIG. 7. Histograms of displacement distributions for all vacuoles in the data set, computed after 1 and 10 time steps Δt for panels (a) and (b), respectively. The bin width in the main plots is set the same; in the inset of panel (b) a larger bin width is used.

vacuole motion at short times may also stem from the viscoelasticity of the amoeba cytoplasm. We also note pronounced zigzag-like variations of $C_{\delta t}(t)$ with the period of one time step, visible at $\delta t/\Delta t = 1$ in Fig. 8. This, once again, relates to the discreteness of recorded vacuole increments visible for the behavior of $P(dx, dt)$

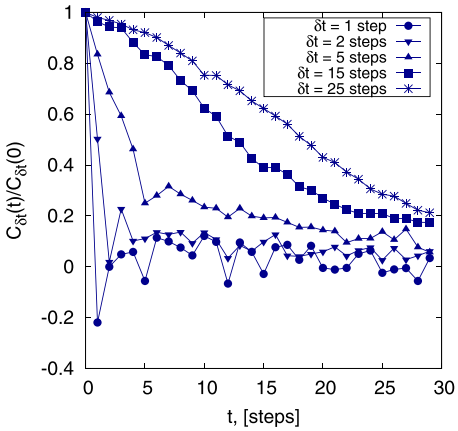

FIG. 8. Displacement autocorrelation function (7) after averaging over all vacuole trajectories. The employed time shifts are listed in the legend.

in Fig. 7. At longer times, the function $C_{\delta t=1}(t)$ reveals fluctuations around zero (possibly, statistically insignificant). A similar behavior of $C_{\delta t}(t)$ at short time-increments δt was detected previously for this system[8] without amoeba locomotion. Note that at short times the negative peak in the velocity autocorrelation function may also emerge due to particle-localization errors and external confinement.[52]

At intermediate and long time shifts δt—when averaging in Eq. (7) is performed largely over a superdiffusive portion of vacuole trajectories—$C_{\delta t}(t)$ attains positive values. Physically, this is an expected behavior for a superdiffusive stochastic process.[12,39,43,44] Namely, the displacements of the tracer at consecutive time steps are positively correlated so that a faster-than-Brownian motion emerges as a result of averaging over many steps. For these larger δt values, the autocorrelation function also reveals a small region of negative values at the respective time values when $t = \delta t$; see Fig. 8. For the regime of substantial time shifts δt and very long times t, the displacement autocorrelation function slowly approaches a small positive value ≈0.1–0.2. This is qualitatively consistent with a weak superdiffusion of vacuoles with $\alpha \approx 1.2$–1.3 observed in this regime; see Fig. 4.[124]

G. Vacuole speeds and locations inside cells

The instantaneous vacuole speeds—defined as elementary vacuole displacements divided over the elementary increment of time in the time series—are distributed, as shown in Fig. 9. The speeds are computed as the modulus of elementary vacuole increments divided by the elementary time step $dt/\Delta t = 1$. In Fig. 9, the speed distributions are shown in terms of fractions of vacuoles in each subpopulation with a given $|v|$ value. The distributions are overall similar for small, medium, and large vacuoles. They all reveal a distinct peak at $|v_{\rm vac}| \approx 0$, additional peaks at $|v_{\rm vac,1}| \approx 1$ μm/s, and small peaks at $|v_{\rm vac}| \approx 0.5$, 1, and 2 μm/s. These peaks complement the peaks in the displacement distribution function after one time step [Fig. 7(a)]. Namely, the zero-speed entries in Fig. 9 correspond to the central peak of $P(dr, dt)$ in Fig. 7(a), while $|v_{\rm vac,\,1}| \sim \frac{0.1\mu\rm m}{0.1\rm s}$ (from one elementary displacement per unit time step Δt). The mean speed—computed via averaging over all increments and all vacuoles—is $\langle|v_{\rm vac}|\rangle \approx 0.5$ μm/s, for all subpopulations of vacuoles.[125]

As mentioned in the Introduction, different motor proteins are abundant on the leading edge of AC cells and in their cytoplasm. Myosin, dynein, and kinesin control the properties of microtubule-based motility of various cell organelles (mitochondria, small particles, granules, lysosomes, vesicles, etc.) over a length-scale of several microns. For mitochondria, for instance, speeds in a range ≈0.5–4 μm/s were recorded.[6] The resolution limits for the tracer's displacements and speeds recorded in flattened, pancake-like AC cells in Ref. 6 were ~0.5 μm and ~0.5 μm/s, correspondingly. As demonstrated in the *in vitro* motility assay, internal AC organelles (mitochondria, small particles, etc.) move at ≈0.4 μm/s toward the plus end and at ≈1.1 μm/s toward the minus end of the microtubule filaments. For the kinesin- and dynein-based modes of transport of (membranous) organelles[32] inside AC cells, the averaged speeds of ≈3.3 and ≈2–3 μm/s were reported in Ref. 6.

The mode of organelle motility in AC cells based on abundant myosin-I motors[9,23]—bound to and "running" along F-actin filaments—can make an additional, sizable contribution.[24] The speed for this mode of transport was reported to be slower, on average ≈0.24 μm/s[24] (see also Ref. 32). The reported transport speeds clearly depend on the detailed experimental conditions and cell-preparation protocols. Therefore, the average instantaneous speeds of (rather large) vacuoles in the range ≈0.5 μm/s we report here are of the same order as the microtubuli-directed traffic speeds for smaller cargos being pulled by different motors, as reported previously.[6,24]

We also examine in Fig. 10 the histogram of vacuole radial distances with respect to the center-of-area of the respective AC cell. Specifically, we compute the distribution $p\left(r = \sqrt{x^2 + y^2}\right)$ over the entire time-tracks of all relative positions of vacuoles $\{x, y\}$. We find

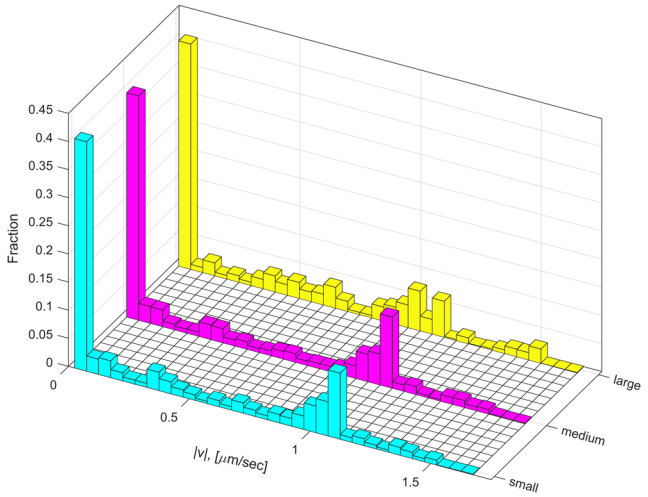

FIG. 9. Instantaneous speeds of vacuoles in terms of percentages of particles with a given $|v|$ value. We emphasize a pronounced peak at $|v| = 0$ corresponding to the displacement distribution peak at $P(dx = 0, dt = 1)$.

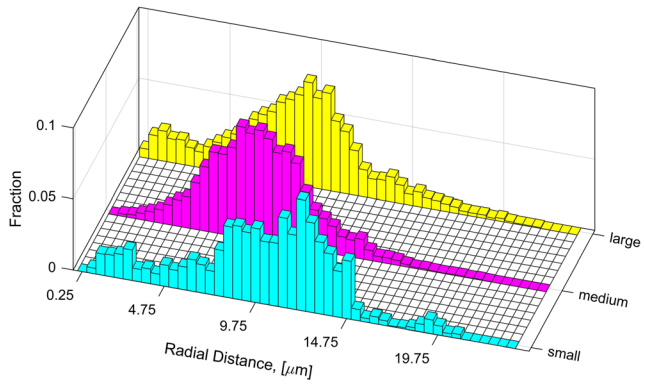

FIG. 10. Radial distribution of vacuoles with respect to the centers of their hosting amoebae (see Fig. 2 for color coding). Fractions with respective radial distances are shown for each subpopulation of vacuoles.

that smaller vacuoles prefer to move closer to the outside/periphery of the cells, as compared to medium and large particles. The latter have the peaks of their position distribution function shifted toward the cell center by ~5 μm. Note that in Fig. 10 the positions of vacuole centers are examined and plotted. This means that larger particles get also effectively "displaced" from the outer cell membrane purely by excluded-volume interactions.[126]

V. DISCUSSION AND CONCLUSIONS

A. Overview and discussion of our main results

In the current study, we quantified the motion of vacuoles inside motile AC cells, see Fig. 1, examining the data sets obtained from SPT experiments using a number of standard[38,39,43–45] statistical quantifiers. Let us summarize our main findings and their interpretation point-by-point below.

(i) We computed and characterized the magnitude and spread of individual TAMSD trajectories for the subpopulations of small, medium, and large vacuoles; see Fig. 2. We revealed that the behavior of the anomalous scaling exponent of the *mean* TAMSD turns from slightly subdiffusive at (very) short lag times to superdiffusive at intermediate lag times. For the later region, a prolonged regime with anomalous diffusion exponent $\langle\beta_{\rm vac}\rangle \approx 1.1$–$1.3$ was detected (Figs. 3 and 4). This motion of vacuoles is superimposed onto a nearly ballistic propulsion of amoebae as such, with MSD exponent $\langle\beta_{\rm AC}\rangle = 1.86 \pm 0.02$ and average speed $|v_{\rm AC}| \approx 0.49$ μm/s; see Fig. 15 in the Appendix. Note that varying the number of fitting points of the TAMSD tracks as well as the size of the data set and its experimental conditions will quantitatively affect the values of $\langle\beta_{\rm AC}\rangle$ and $\langle\beta_{\rm vac}\rangle$. The reported spread of $\overline{\delta_i^2(\Delta)}$ trajectories is also going to be affected; see Refs. 12, 56, 58, 59, and 77 for the discussion.

We emphasize here that apparent weak subdiffusion[52,72,78–81] observed at very short lag times can be induced by the localization error of vacuoles in these SPT experiments; see also note.[69] A subdiffusive behavior—instead of Brownian diffusion for $\overline{\delta_i^2(\Delta)}$ displacements—would then emerge at short lag times solely due to particle-localization uncertainties, as predicted and quantified theoretically in Ref. 78. Specifically, the "flattening" of the TAMSDs is pronounced at short times, with the predicted TAMSD expression being (for normal basal diffusion) $\left\langle\overline{\delta^2(\Delta)}\right\rangle \sim 2\sigma^2 + 2D\Delta$; see Refs. 52, 78, and 79. Here, $\sigma \approx 1$–2 pixels is the *static* localization error of the particle in SPT experiments; see also Sec. II. Indeed, the vacuole displacements at short lag times—namely, $\left\langle\overline{\delta_{\rm vac}^2}\right\rangle \sim (0.1\ \mu{\rm m})^2$ as seen from Fig. 3—are comparable to the resolution of the current SPT setup. Additionally, a finite camera-exposure time gives rise to motion blurring of the tracers and associated *dynamic* localization error; see the discussion in Refs. 58, 72, 79, and 82.

Similar features of the short-time behavior of $\overline{\delta_i^2(\Delta)}$ reported in Ref. 8 can have similar localization-error-related origin. Note, however, that in Ref. 8 the experimental settings and the analysis algorithm were different (with regard to center-of-area tracking, methods of vacuole tracking, etc.).

(ii) We observed that at the start of the vacuole trajectories the values of the trace-specific diffusion coefficient and scaling exponent are *positively* correlated; see Fig. 5. This reflects the physical picture of vacuoles with small (large) exponents featuring small (large) diffusion coefficients at the initial stage of diffusion. At later stages, these correlations virtually disappear and, finally, turn *negative*. Below, we discuss some physical reasons for this surprising behavior of K_β–β correlations.

First, large variability of cell sizes, dynamic changes of shapes of cells and vacuoles, as well as polydispersity of vacuole dimensions, together with heterogeneous crowding of the cytoplasm, make the current system quite complicated to study, both in terms of the SPT experiments and the statistical analysis. Mutual correlations of diffusivities and exponents as well as peculiar features of the distribution of diffusivities, $p(K_\beta)$, may stem from multiple complicated mechanisms controlling the vacuole motion. Their deeper understanding will deliver new insights regarding underlying stochastic processes as well as physical effects of the medium onto vacuole diffusion (confinement/caging, binding-unbinding dynamics, medium viscoelasticity, etc.,). Note also that certain issues of heterogeneous crowding and anomalous space-dependent diffusion can also be at play here, as investigated recently for cell-mimicking bounded domains, both theoretically and by computer simulations.[74,84,85]

Recently, for more size-restricted and controlled diffusion of calibrated nanoparticles in the cytoplasm of live mammalian cells, pronounced variations and *different* inter-relations between K_β and β were reported.[56] Variable nanoparticle sizes (from 25 to 75 nm) and their nonspecific interactions[83] with the medium were examined.[56] These and other experimental features were shown to affect[56] the observed K_β–β correlations, often turning out to be *positive*, similar to our Fig. 5.

The vacuoles inside amoebae are highly confined due to the cell envelope. To mimic this, we simulated harmonically confined passive particles, the so-called Ornstein-Uhlenbeck process.[63,86] For this process, we unveiled similar K_β–β correlations: *pronouncedly positive* at short times, turning *strongly negative* at later times; see Fig. 18 in the Appendix. The confined motion is realized at times much longer than the internal correlation time of this diffusion process, $1/\lambda$.[63] Thus, a confined motion is consistent with a transition from positive to negative correlations observed at later stages of vacuole motion in AC cells; see Fig. 17 in the Appendix.

(iii) From the behavior of the TAMSDs of vacuoles, we observe that their diffusion is strongly non-Brownian.[39,43] The ergodicity breaking parameter was computed after averaging over vacuoles of all sizes in the data set (Fig. 6). The evolution of EB(Δ) demonstrates that vacuole motion is nonergodic. Despite rather high and nonvanishing EB values at short lag times, the magnitudes of the MSD and mean TAMSDs for the vacuole trajectories are close; see Fig. 16 in the Appendix. Note that similar features were observed in the simulations of Ref. 71. Moreover, the decay of the EB parameter at short lag times with the length of trajectories was shown to be slower than ${\rm EB}(T) \propto 1/T$; see the inset of Fig. 6. (Note that similar sublinear EB behaviors with 1/T were reported recently for the models of diffusion in heterogeneous media[87] and in computer simulations of lipid diffusion in membranes with dynamic interactions.[71] Both these systems involve the concept of "diffusing diffusivity;" see Refs. 71, 76, 77, and 88–94 for an overview.)

As we mentioned previously,[43,65] the requirements on the size of the data set for computing the higher-order moments of particle displacements, such as the EB parameter, are much stricter

compared to those for the second moments, such as $\overline{\delta^2}$. Many more SPT trajectories—recorded (at best) at identical experimental conditions and minimal polydispersity of cell and vacuole sizes—are needed to make a confident conclusion regarding the EB scaling behavior for vacuole inter-cellular motion as a function of lag time Δ and trajectory length T (work in progress).

Note also that additional issues—varying sample size, minimal trajectory length, uniform versus non-uniform distribution of track lengths used in the analysis, and varying vacuole sizes and amoeba speeds—can all affect the final results of the analysis; see Refs. 65, 68, and 95 for the discussion. How strong the effects of the diffusion environment is onto the observed properties of the TAMSD and the EB parameter of vacuole motion and how much is due to sample-acquisition limitations, experimental restrictions, and sample-set properties is to be examined in the future.[96]

(iv) We computed the distributions of vacuole displacements with respect to the center-of-area of respective amoebae, at varying time shifts from the start of the measurement; see Fig. 7(a). We observed strongly non-Gaussian pixel-size-dependent vacuole displacement-distributions, for individual Cartesian x-y coordinates as well as the radial displacements, $p\left(r = \sqrt{x^2 + y^2}\right)$. For instance, after a single step of diffusion ($dt = 1$), we detected a peak of vacuole displacements at $dx = dy = 0$ supplemented by two smaller peaks at the increments of $dx = dy = \pm 1$ pixel size. These discreteness effects persist also at later stages of vacuole diffusion; see Fig. 7(b) and note.[69]

(v) We computed the displacement autocorrelation function $C_{\delta t}(t)$ along individual trajectories of vacuoles [Eq. (7)]. The results we presented in Fig. 8 indicate the presence of pixel-size effects, particularly at minimal time shift $\delta t = 1$, as expected. Also, as the data set was rather limited, we observed pronounced fluctuations in the behavior of $C_{\delta t=1}(t)$ at later times t. For longer time shifts δt, the pixel-size effects were smoothened and the reported $C_{\delta t}(t)$ function revealed a monotonic decay from unity toward a small positive value. This is consistent with a slightly superdiffusive nature of vacuole motion in this time domain. The pixel-size effects manifest themselves also in the distribution of instantaneous speeds of vacuoles, as seen from Fig. 9.[127,128]

The novelty of the current study from the *experimental* point of view is in successful recording of much longer trajectories via constructing an automated tracking system on the microscope. Previously,[8] the AC cells leaving the image resulted in terminated SPT-tracks, which also caused certain bias in the data. Namely, longer vacuole trajectories remained in the set mainly stemmed from slower amoebae staying in the image longer. From the *data-analysis* viewpoint—as compared to Refs. 8—the novel elements are, in particular, the study of cross correlations K_β–β and the distribution of generalized diffusion coefficients $p(K_\beta)$, the behavior of the EB parameter, and the spatial distribution of vacuoles inside AC cells. Some of these examinations as well as the TAMSD calculations were performed separately for subpopulations of small, medium, and large vacuoles. Thus, the current analysis delivers new insight into the mechanisms of diffusion of polydisperse vacuoles inside motile amoebae. Our results may help unveil certain features of the amoeba functions and its pathogenetic activity connected with vacuole motion, as outlined in Sec. I.

B. Possible models and mechanisms of vacuole diffusion

Some recent studies employed similar statistical quantifiers aiming at predicting the most-probable model of diffusion using the time series from various SPT-experiments as input signals.[12,37,50,51,54,56,65,77,97] The "best" model of diffusion has to accommodate various features of tracer motion often observed in SPT-experiments, such as anomalous, non-ergodic, non-Gaussian, and (possibly) aging features of diffusion. Physically, such a model should reflect the underlying transport features and particle-trapping mechanisms imposed by the medium. The models of continuous-time random walks, fractional Brownian motion, generalized Langevin equation motion, multi-state diffusion, and diffusing-diffusivity have been proposed (among others) as—sometimes conflicting—candidates for rationalizing experimental SPT observations.[12,39–41,43,45,50,51,54,65,71,90,95,98–101] In addition to ensemble-averaged properties, some single-trajectory-based quantifiers were also proposed recently for confident selection, validation, and discrimination of different anomalous diffusion models (see Ref. 101 for the sample characteristic function, mixing, and ergodicity estimators). We also emphasize here the recent power-spectral-density approach of Ref. 22 that was successfully applied to the experimental data of vacuole diffusion inside AC cells.

For instance, our recent Bayesian analysis[65,77] demonstrated that SPT trajectories of tracer particles in polymeric mucin gels may be well mimicked by Brownian or fractional Brownian type of motion. The spread of individual $\overline{\delta_i^2(\Delta)}$ trajectories observed for an ensemble of tracers should then be accounted for in the analysis via additional inter-relations between certain diffusive characteristics. These can be, e.g., the distribution of and the correlations between the values of the diffusion coefficient and scaling exponent, such as those observed in Fig. 19 in the Appendix and Fig. 5. These dependencies reflect the impact of physical interactions and processes at play for a given system.

Generally, mathematical models of different degrees of complexity may be proposed to describe experimental SPT observations. Ideally, the principles of Bayesian statistics and Occam's razor should be employed[77,102–104] to rank plausible theoretical models. Specifically, models with excessive numbers of parameters or parameter-distribution embeddings should be penalized (despite better data fits they might produce). As another extreme, choosing a physically simplistic model often results in neglecting important biological details of the system so that vital dependencies on tunable experimental parameters cannot be captured, for instance.

Statistical diffusion models of *hierarchical nature*—such as superstatistics[90,93,105,106]—can also be proposed, in which the dynamics of model parameters on multiple scales in space and time gets superposed or convoluted with the original propagator of a given model of diffusion. The mathematically powerful concepts of superstatistics—although offering fits to the observed behaviors of, e.g., $P(x, t)$ and the TAMSDs—may, however, still lack a clear physical rationale for the observed behavior; see the examples in Ref. 102. Similar caution is required when providing physical interpretations of SPT observations using the concepts of ensemble-distributed, time-local, and time-random or diffusing model parameters, such as diffusing diffusivity.[54,71,88,90,107] Heterogeneous diffusion[74,87,99,102,108,109]—as a superposition of

simple ergodic diffusion with distributed model parameters—can be also of relevance for the current data. Such a hierarchical embedding of distributions of parameters into a standard diffusion model can give rise, e.g., to a multitude of non-Gaussian density-distribution functions.[90,93,102]

The vacuoles—during a finite diffusion time in our experiments—do not manage to sample the entire cell uniformly. Due to size variations, certain processes of active and passive nature can differ from vacuole to vacuole. Additionally, the vacuoles experience different intercellular conditions during highly motile AC motion and due to heterogeneity of its cytoplasm. Therefore, some distributions of model parameters can be involved into the models—in the superstatistical sense—on multiple levels. These may mimic, e.g., an ensemble of non-identical particles or varying environments for vacuole subpopulations (see Ref. 65).

A motor-driven component of vacuole transport can be present in the current data. It is, however, currently not clear to what extent the network of "cytoskeletal-based highways" stays intact in the course of AC locomotion. This affects how viable the cytoskeletal elements are as the transducers of amoeba motion in terms of creating cytoplasmic flows and streams;[20] see also the supplementary material video files in real time. At the moment it is not clear whether the vacuoles are evolving with the cell membrane which is rolling-over upon amoeba motion (the "rotating wheel" analogy). Also, how strongly the vacuoles of different sizes are involved in microtubuli- and actin-based transport is currently not clear.

Yet, a two-state active and passive diffusion model may be realistic for vacuole motion. The passive diffusivity of vacuoles can depend, i.e., on their radial distance in the AC cell, vacuole size, and cell-locomotion speed in a model with *ab initio* Gaussian displacements, $D_{\rm pas} = D_{\rm pas}(r, R_{\rm vac}, |v_{\rm AC}|)$. Likewise, for the active (motor-driven) mode of vacuole motion, one sets $D_{\rm act} = D_{\rm act}(r, R_{\rm vac}, |v_{\rm AC}|)$. Additionally, the distributions of diffusion times that vacuoles spend in each of these modes should be parameterized. [Such a system with two diffusivities (see Ref. 110 and also later studies[101,111,112]) is reminiscent of "hopping-and-sliding" diffusion of DNA-binding proteins searching for targets on DNA.[113–115]] To unveil the properties of vacuole binding-unbinding kinetics and active-to-passive switchings from individual time series, more delicate methods may be needed; see, e.g., Refs. 101 and 112. Different states for multi-state diffusion processes[71,112] as well as certain separation of particles into subpopulations may be required to quantify these features. Moreover, time-local diffusivity of vacuoles along their tracks can be analyzed to detect two-state diffusion (see the method of Ref. 71).

C. Discussion of directions of future research

Clearly, a number of additional quantifiers—both for the ensemble-averaged and single-trajectory-based properties of recorded time series—can be employed in a more extended analysis; see, e.g., Refs. 12, 22, 65, 101, and 116. For instance, one additional property we unveiled for one of the four AC cells is *positive correlations* in the directions of motion of vacuoles and amoebae hosting them (Fig. 20 in the Appendix). We find that the discreteness of vacuole displacement (as seen in Fig. 7, see also Ref. 69) also gets reflected in certain preferred/discretized directions of vacuole azimuthal motion, as examined from the increments after one time step, $dt/\Delta t = 1$. Although some amoebae do reveal correlations in motion with their internalized vacuoles, see Fig. 20 in the Appendix, larger sample sizes are crucial to understand this in depth. Such directional correlations render slightly superdiffusive motion of vacuoles inside highly motile amoebae—as we observe in a certain window of lag times in Fig. 3—plausible also without active mechanisms of cytoplasmic transport. The mechanism of superdiffusive transport of vacuoles is thus—at least partly—due to persistence of motion of AC cells themselves (a model of diffusion with a constant drift).

In addition to a possible "wheel effect," locomotive amoebae can create internal membrane-originating[19] *flows* involving cytoplasmic components, including vacuoles. These flows are known to be pronounced for other locomotive cells (see also the video files in the supplementary material). For instance, the flow velocities of up to 40% of the cell velocity in the direction of the leading-edge were detected for rapidly moving fish epithelial keratocyte cells in Ref. 13. The flows of cytoplasmatic fluid were quantified[13] for the probes of various sizes diffusing in thin lamellipodia of these highly persistent keratocytes[13] (average speed of $\approx 0.3\ \mu$m/s). Surprisingly, however, only slightly subdiffusive spreading of small quantum dots was detected in the lamellipodia in the reference frame of the cell.[13] Namely, the exponent was found to be $\alpha \approx 0.89$, with the tracer dynamics featuring large variations (in terms of trajectory-specific diffusivities).[13] Interestingly, the flow-induced concentration of larger probes near the leading edge in these cells was larger than that of small probes (30-nm quantum dots).[13] Blebbistatin-treated cells did not change severely the behavior of the leading edge but rather affected the intercellular fluid flows and hydrostatic-pressure gradients from the front to the rear end of the cell.

Anomalous, heterogeneous, and non-Gaussian diffusion—with a certain degree of cell-to-cell variability and cell-size-dependent particle diffusivity—was recently reported for the spreading dynamics of intrinsically polymerizing H-NS proteins in live *Escherichia coli*; see Ref. 73. Projecting to our data set, a differentiation of AC cells based on their size can shed light on certain diffusive properties of internal vacuoles. A much larger sample of trajectories from different and well controlled cells is, however, required to draw statistically meaningful conclusions here. For instance, one can ask whether larger cells host, on average, faster vacuoles (Fig. 16 in the Appendix).

Note that different degrees of *compression* of amoebae toward the surface can also affect the magnitude and exponent of the TAMSD trajectories of vacuoles. In these lines, for instance, a dramatic reduction in the TAMSD (at a constant exponent) was recently reported[97] for diffusion of DNA chromosomal loci in compressed *Escherichia coli* cells. Additional dynamic fluctuations of shapes and sizes of vacuoles also impact their diffusive properties (see also the discussion in Ref. 71).

Finally, and quite naturally, the physical mechanisms of two-dimensional motion of AC cells on adhesive supports may differ[16,117] from those for many natural three-dimensional media. The tracking process in three dimensions may, however, be very challenging; see Ref. 118 for the recent SPT advances. More sophisticated tracking methods[67,104,118] may help unveil new details of functioning of this pathogenic system. Such methods should

have a better localization precision of vacuoles, higher recording frequencies, smaller effects of cell-to-cell variability, advanced vacuole-size control, as well as better control over possible noise sources (vibrations of the setup table, fluctuations of the light intensity, etc.). These questions point the directions for future research.

SUPPLEMENTARY MATERIAL

See supplementary material for videos.

ACKNOWLEDGMENTS

A.G.C. acknowledges E. P. Petrov for stimulating discussions. The authors thank the careful referees for their insightful comments. R.M. acknowledges financial support from the Deutsche Forschungsgemeinschaft (DFG Grant Nos. ME 1535/6-1 and ME 1535/7-1). R.M. also thanks the Foundation for Polish Science within an Alexander von Humboldt Polish Honorary Research Fellowship. S.T. acknowledges the Deutscher Akademischer Austauschdienst for a Ph.D. Scholarship (DAAD Program No. 57214224). N.L. thanks the DFG for funding through the Collaborative Research Center CRC 1261.

There are no conflicts of interest to declare.

APPENDIX: SUPPLEMENTARY FIGURES

In this appendix we present Figs. 11–21 supporting the claims in the main text of the paper.

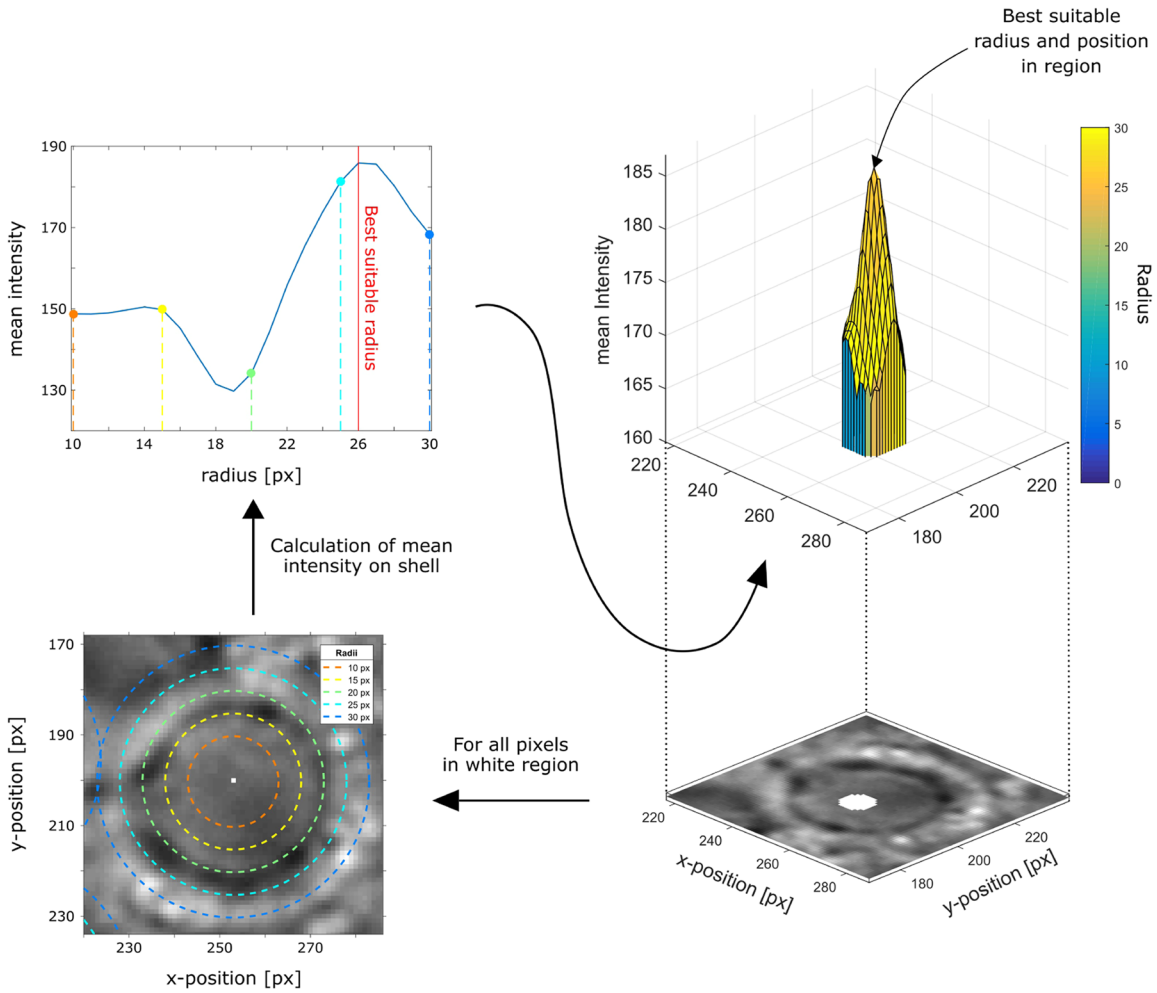

FIG. 11. Intermediate steps and methodology for determining the radii and respective center positions of AC vacuoles.

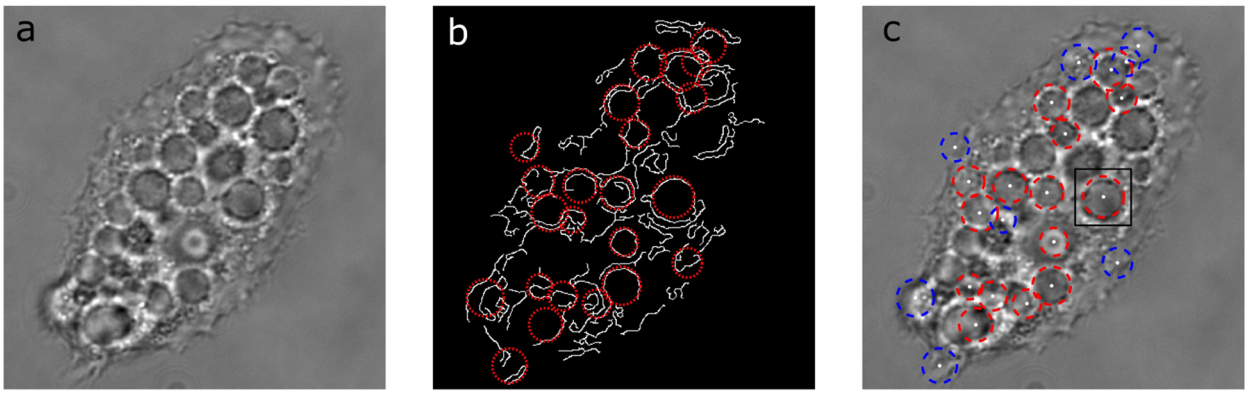

FIG. 12. Determined radii and center positions of AC vacuoles, see also Fig. 11.

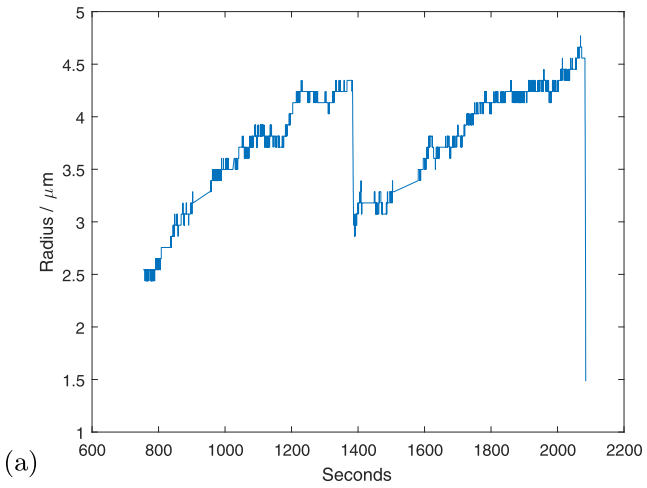

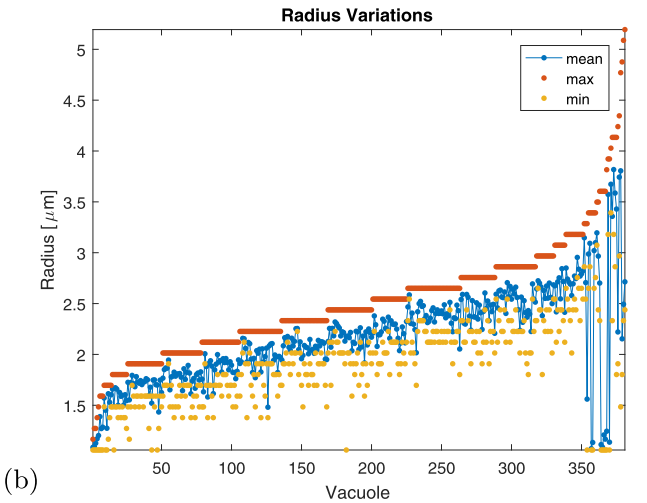

FIG. 13. (a) abrupt changes of the radius of one of the largest vacuole (see amoeba #1 video in the supplementary material) and (b) variations of radii recorded along the vacuole trajectories, ordered in the plot from the smallest to the largest maximal radius for each vacuole. Maximal, minimal, and mean radii are shown in the graph (see the legend).

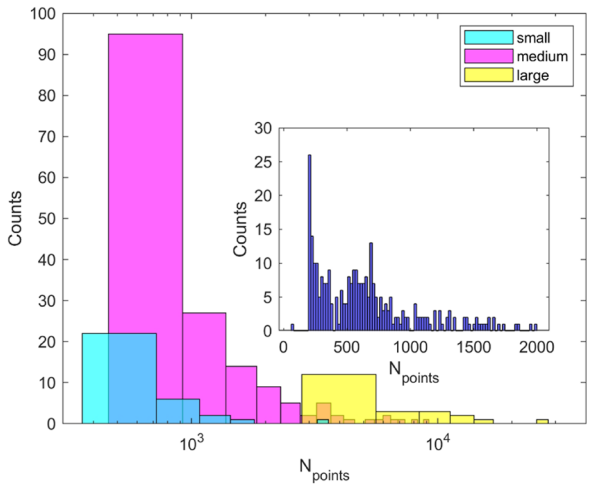

FIG. 14. Distributions of trajectory lengths $T = N_{\text{points}} \times \Delta t$ for subpopulations of vacuoles (one time step is $\Delta t \approx 1/9$ s). The legend shows the separation of vacuoles by sizes (with the color scheme used in Fig. 2). The inset shows the entire trace-length distribution (without division into subpopulations of vacuoles) on a linear scale.

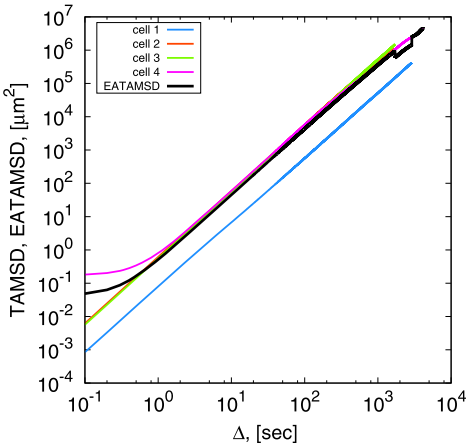

FIG. 15. Nearly ballistic motion of the center-of-area of four AC cells, with the mean exponent computed to be $\langle \beta_{AC} \rangle = 1.86 \pm 0.02$.

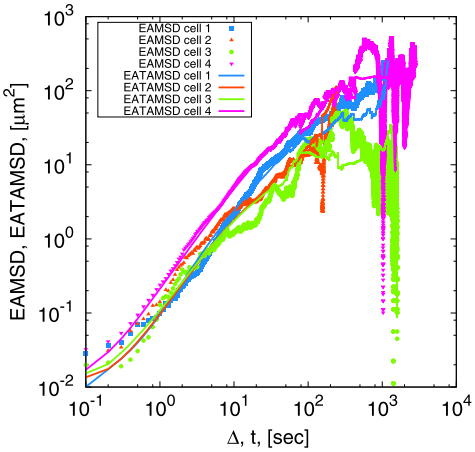

FIG. 16. MSDs (1) and mean TAMSDs (3) computed separately for vacuole diffusion inside each of four amoebae.

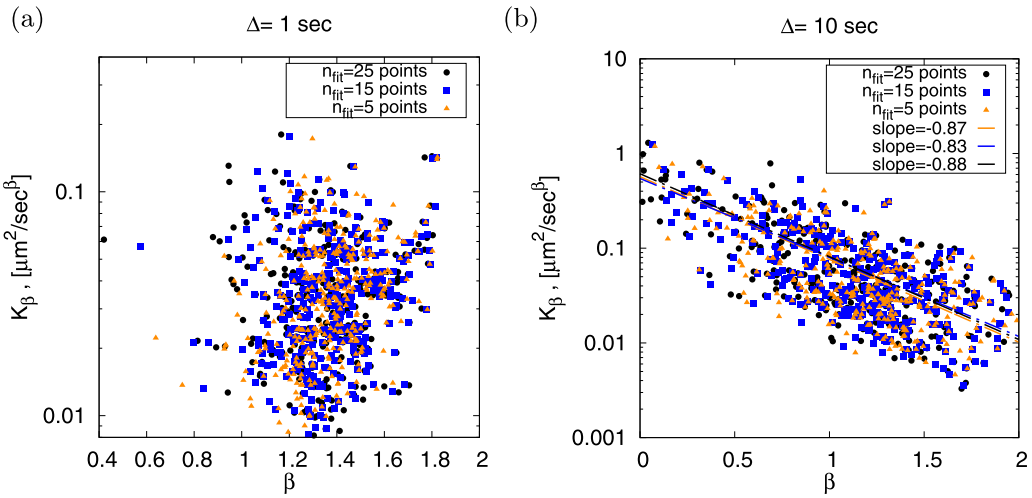

FIG. 17. The same as in Fig. 5 but at Δ_{start} = 1 s [panel (a)] and Δ_{start} = 10 s [panel (b)].

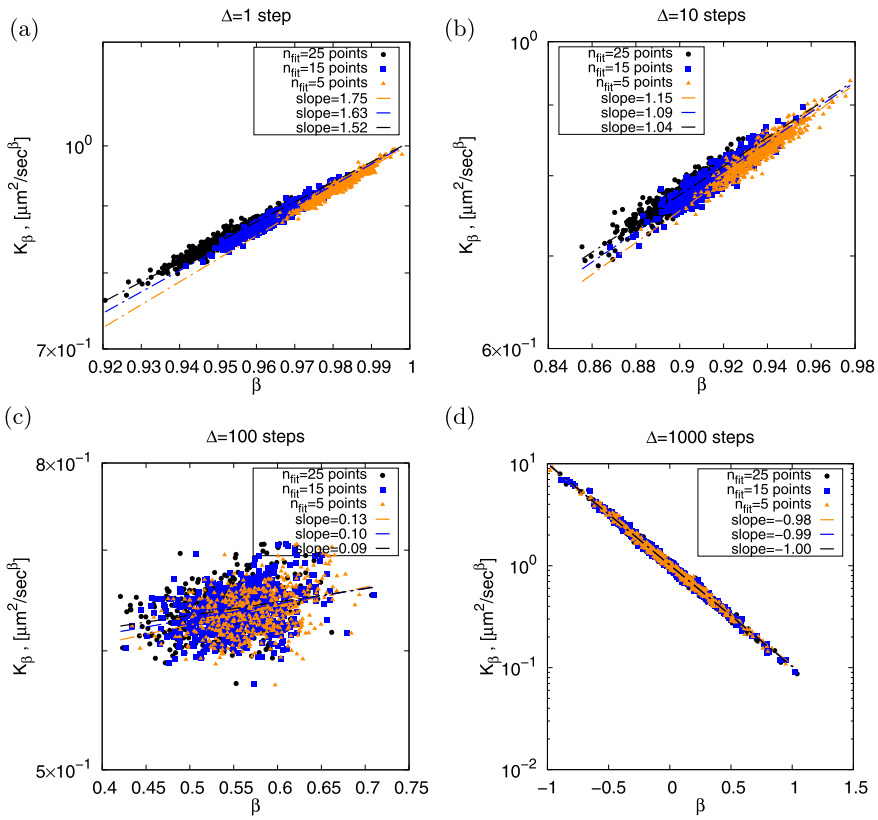

FIG. 18. The same as in Fig. 5 but for the *in-silico*-generated trajectories of the Ornstein-Uhlenbeck process at lag times $\Delta_{start} = 10^0, 10^1, 10^2, 10^3$. Parameters: the relaxation time is $1/\lambda = 1$, the number of trajectories is $N = 500$, and the trace length is $T = 10^5$ steps. The initial positions of particles, x_0, were chosen at equilibrium $p(x_0) = e^{-x_0^2/2}/\sqrt{2\pi}$, see Ref. 63 for details.

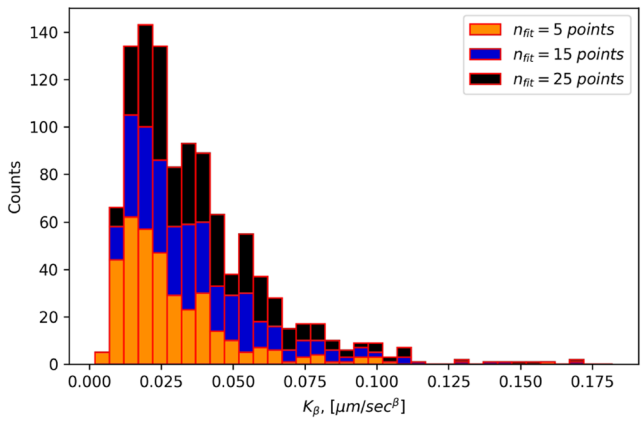

FIG. 19. Distribution of generalized diffusion coefficients measured at short lag times for vacuole motion. The results are presented as *stacked* histograms (the bins do not overlap).

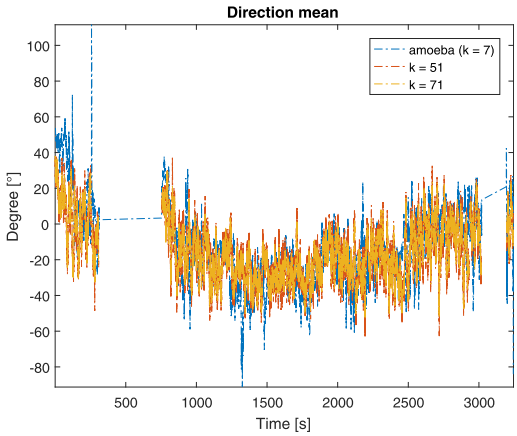

FIG. 20. Correlations in directions of motion for amoeba #1 and all its internalized vacuoles. The trajectories of the amoeba and of the vacuoles were smoothened here over the number of time steps *k*, as listed in the legend. The angles of motion for amoeboid cells and their internal vacuoles are defined clockwise, starting from the direction to the right that is assigned as zero-angle motion in the SPT videos.

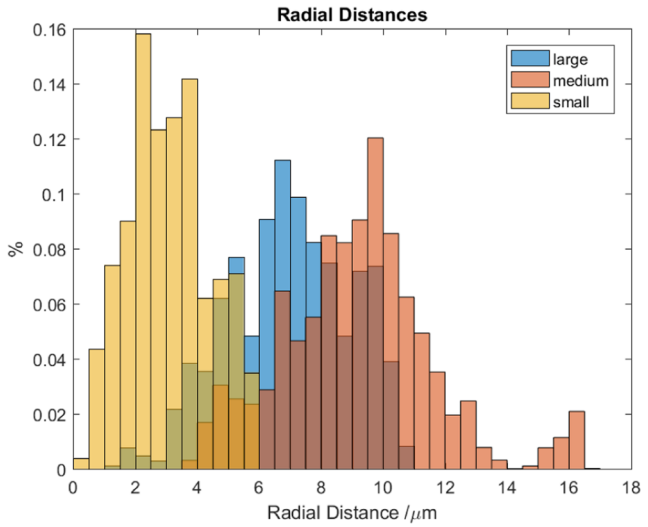

FIG. 21. The same as in Fig. 10 but with mean (and not maximum) vacuole radii used in the analysis [see Fig. 13(b)].

REFERENCES

[1]F. Marciano-Cabral and G. Cabral, "*Acanthamoeba* spp. as agents of disease in humans," Clin. Microbiol. Rev. **16**, 273 (2003).

[2]N. Khan, *Acanthamoeba: Biology and Pathogenesis* (Calster Academic Press, 2009).

[3]N. A. Khan, "*Acanthamoeba*: Biology and increasing importance in human health," FEMS Microbiol. Rev. **30**, 564 (2006).

[4]V. Thomas, G. McDonnell, S. P. Denyer, and J.-Y. Maillard, "Free-living amoebae and their intracellular pathogenic microorganisms: Risks for water quality," FEMS Microbiol. Rev. **34**, 231 (2010).

[5]B. Bowers and E. D. Korn, "The fine structure of *Acanthamoeba castellanii* I," J. Cell Biol. **39**, 95 (1968).

[6]O. Baumann and D. B. Murphy, "Microtubule-associated movement of mitochondria and small particles in *Acanthamoeba castellanii*," Cell Motil. Cytoskel. **32**, 305 (1995).

[7]B. Bowers and E. D. Korn, "The fine structure of *Acanthamoeba castellanii* II," J. Cell Biol. **41**, 786 (1969).

[8]J. F. Reverey, J.-H. Jeon, H. Bao, M. Leippe, R. Metzler, and C. Selhuber-Unkel, "Superdiffusion dominates intracellular particle motion in the supercrowded cytoplasm of pathogenic *Acanthamoeba castellanii*," Sci. Rep. **5**, 11690 (2015).

[9]S. K. Doberstein, I. C. Baines, G. Wiegand, E. D. Korn, and T. D. Pollard, "Inhibition of contractile vacuole function *in vivo* by antibodies against myosin-I," Nature **365**, 841 (1993).

[10]D. J. Patterson, "Contractile vacuoles and associated structures: Their organization and function," Biol. Rev. **55**, 1 (1980).

[11]H.-F. Hsu, E. Bodenschatz, C. Westendorf, A. Gholami, A. Pumir, M. Tarantola, and C. Beta, "Variability and order in cytoskeletal dynamics of motile amoeboid cells," Phys. Rev. Lett. **119**, 148101 (2017).

[12]A. G. Cherstvy, O. Nagel, C. Beta, and R. Metzler, "Non-Gaussianity, population heterogeneity, and transient superdiffusion in the spreading dynamics of amoeboid cells," Phys. Chem. Chem. Phys. **20**, 23034 (2018).

[13]K. Keren, P. T. Yam, A. Kinkhabwala, A. Mogilner, and J. A. Theriot, "Intracellular fluid flow in rapidly moving cells," Nat. Cell Biol. **11**, 1219 (2009).

[14]J. A. Theriot and T. J. Mitchison, "Actin microfilament dynamics in locomoting cells," Nature **352**, 126 (1991).

[15]T. J. Mitchison and L. P. Cramer, "Actin-based cell motility and cell locomotion," Cell **84**, 371 (1996).

[16]E. Tjhung, A. Tiribocchi, D. Marenduzzo, and M. E. Cates, "A minimal physical model captures the shapes of crawling cells," Nat. Commun. **6**, 5420 (2015).

[17]C. Manzo and M. F. Garcia-Parajo, "A review of progress in single particle tracking: From methods to biophysical insights," Rep. Prog. Phys. **78**, 124601 (2015).

[18]U. S. Schwarz and S. A. Safran, "Physics of adherent cells," Rev. Mod. Phys. **85**, 1327 (2013).

[19]K. Keren, "Cell motility: The integrating role of the plasma membrane," Eur. Biophys. J. **40**, 1013 (2011).

[20]Y. Cao *et al.*, "Cell motility dependence on adhesive wetting," Soft Matter **15**, 2043 (2019).

[21]J. Steinwachs, C. Metzner, K. Skodzek, N. Lang, I. Thievessen, C. Mark, S. Münster, K. E. Aifantis, and B. Fabry, "Three-dimensional force microscopy of cells in biopolymer networks," Nat. Methods **13**, 171 (2016).

[22]D. Krapf, N. Lukat, E. Marinari, R. Metzler, G. Oshanin, C. Selhuber-Unkel, A. Squarcini, L. Stadler, M. Weiss, and X. Xu, "Spectral content of a single non-Brownian trajectory," Phys. Rev. X **9**, 011019 (2019).

[23]T. D. Pollard and E. D. Korn, "*Acanthamoeba* myosin. I. Isolation from *Acanthamoeba castellanii* of an enzyme similar to muscle myosin," J. Biol. Chem. **248**, 4682 (1973); available at http://www.jbc.org/content/248/13/4682.abstract.

[24]R. J. Adams and T. D. Pollard, "Propulsion of organelles isolated from *Acanthamoeba* along actin filaments by myosin-I," Nature **322**, 754 (1986).

[25]B. Alberts, A. Johnson, J. Lewis, D. Morgan, M. Raff, K. Roberts, and P. Walter, *Molecular Biology of the Cell*, 6th ed. (Garland Science, New York, 2014).

[26]F. Jülicher, A. Ajdari, and J. Prost, "Modeling molecular motors," Rev. Mod. Phys. **69**, 1269 (1997).

[27]A. B. Kolomeisky and M. E. Fisher, "Molecular motors: A theorist's perspective," Annu. Rev. Phys. Chem. **58**, 675 (2007).

[28]B. Kachar, E. C. Bridgman, and T. S. Reese, "Dynamic shape changes of cytoplasmic organelles translocating along microtubules," J. Cell Biol. **105**, 1267 (1987).

[29]K. Chen, B. Wang, and S. Granick, "Memoryless self-reinforcing directionality in endosomal active transport within living cells," Nat. Mater. **14**, 589 (2015).

[30]F. Jülicher, K. Kruse, J. Prost, and J.-F. Joanny, "Active behavior of the cytoskeleton," Phys. Rep. **449**, 3 (2007).

[31]T. A. Schroer, E. F. Steuer, and M. P. Sheetz, "Cytoplasmic dynein is a minus end-directed motor for membranous organelles," Cell **56**, 937 (1989).

[32]N. Hirokawa, "Kinesin and dynein superfamily proteins and the mechanism of organelle transport," Science **279**, 519 (1998).

[33]A. J. Roberts, T. Kon, P. J. Knight, K. Sutoh, and S. A. Burgess, "Functions and mechanics of dynein motor proteins," Nat. Rev. Mol. Cell Biol. **14**, 713 (2013).

[34]N. Bettache, L. Baisamy, S. Baghdiguian, B. Payrastre, P. Mangeat, and A. Bienvenue, "Mechanical constraint imposed on plasma membrane through transverse phospholipid imbalance induces reversible actin polymerization via phosphoinositide 3-kinase activation," J. Cell Sci. **116**, 2277 (2003).

[35]L. Yan, R. L. Cerny, and J. D. Cirillo, "Evidence that hsp90 is involved in the altered interactions of *Acanthamoeba castellanii* variants with bacteria," Eukaryotic Cell **3**, 567 (2004).

[36]See https://tinevez.github.io/msdanalyzer/ for the @msdanalyzer procedure.

[37]P. Struntz and M. Weiss, "The hitchhiker's guide to quantitative diffusion measurements," Phys. Chem. Chem. Phys. **20**, 28910 (2018).

[38]Y. He, S. Burov, R. Metzler, and E. Barkai, "Random time-scale invariant diffusion and transport coefficients," Phys. Rev. Lett. **101**, 058101 (2008).

[39]S. Burov, J.-H. Jeon, R. Metzler, and E. Barkai, "Single particle tracking in systems showing anomalous diffusion: The role of weak ergodicity breaking," Phys. Chem. Chem. Phys. **13**, 1800 (2011).

[40]J.-H. Jeon, V. Tejedor, S. Burov, E. Barkai, C. Selhuber-Unkel, K. Berg-Sørensen, L. Oddershede, and R. Metzler, "*In vivo* anomalous diffusion and weak ergodicity breaking of lipid granules," Phys. Rev. Lett. **106**, 048103 (2011).

[41]I. M. Sokolov, "Models of anomalous diffusion in crowded environments," Soft Matter **8**, 9043 (2012).

[42]F. Höfling and T. Franosch, "Anomalous transport in the crowded world of biological cells," Rep. Prog. Phys. **76**, 046602 (2013).
[43]R. Metzler, J.-H. Jeon, A. G. Cherstvy, and E. Barkai, "Anomalous diffusion models and their properties: Non-stationarity, non-ergodicity, and ageing at the centenary of single particle tracking," Phys. Chem. Chem. Phys. **16**, 24128 (2014).
[44]R. Metzler, J.-H. Jeon, and A. G. Cherstvy, "Non-Brownian diffusion in lipid membranes: Experiments and simulations," Biochim. Biophys. Acta **1858**, 2451 (2016).
[45]K. Nørregaard, R. Metzler, C. Ritter, K. Berg-Sørensen, and L. Oddershede, "Manipulation and motion of organelles and single molecules in living cells," Chem. Rev. **117**, 4342 (2017).
[46]I. Golding and E. C. Cox, "Physical nature of bacterial cytoplasm," Phys. Rev. Lett. **96**, 098102 (2006).
[47]A. Caspi, R. Granek, and M. Elbaum, "Enhanced diffusion in active intracellular transport," Phys. Rev. Lett. **85**, 5655 (2000).
[48]S. Banks and C. Fradin, "Anomalous diffusion of proteins due to molecular crowding," Biophys. J. **89**, 2960 (2005).
[49]J. Szymanski and M. Weiss, "Elucidating the origin of anomalous diffusion in crowded fluids," Phys. Rev. Lett. **103**, 038102 (2009).
[50]A. V. Weigel, B. Simon, M. M. Tamkun, and D. Krapf, "Ergodic and nonergodic processes coexist in the plasma membrane as observed by single-molecule tracking," Proc. Natl. Acad. Sci. U. S. A. **108**, 6438 (2011).
[51]S. C. Weber, A. J. Spakowitz, and J. A. Theriot, "Bacterial chromosomal loci move subdiffusively through a viscoelastic cytoplasm," Phys. Rev. Lett. **104**, 238102 (2010).
[52]S. C. Weber, M. A. Thompson, W. E. Moerner, A. J. Spakowitz, and J. A. Theriot, "Analytical tools to distinguish the effects of localization error, confinement, and medium elasticity on the velocity autocorrelation function," Biophys. J. **102**, 2443 (2012).
[53]J.-H. Jeon, N. Leijnse, L. B. Oddershede, and R. Metzler, "Anomalous diffusion and power-law relaxation of the time averaged mean squared displacement in worm-like micellar solutions," New J. Phys. **15**, 045011 (2013).
[54]T. J. Lampo, S. Stylianidou, M. P. Backlund, P. A. Wiggins, and A. J. Spakowitz, "Cytoplasmic RNA-protein particles exhibit non-Gaussian subdiffusive behavior," Biophys. J. **112**, 532 (2017).
[55]G. Seisenberger, M. U. Ried, T. Endre, H. Büning, M. Hallek, and C. Bräuchle, "Real-time single-molecule imaging of the infection pathway of an adeno-associated virus," Science **294**, 1929 (2001).
[56]F. Etoc, E. Balloul, C. Vicario, D. Normanno, D. Liße, A. Sittner, J. Piehler, M. Dahan, and M. Coppey, "Non-specific interactions govern cytosolic diffusion of nanosized objects in mammalian cells," Nat. Mater **17**, 740 (2018).
[57]M. S. Song, H. C. Moon, J.-H. Jeon, and H. Y. Park, "Neuronal messenger ribonucleoprotein transport follows an aging Lévy walk," Nat. Commun. **9**, 344 (2018).
[58]X. Michalet, "Mean square displacement analysis of single-particle trajectories with localization error: Brownian motion in an isotropic medium," Phys. Rev. E **82**, 041914 (2010).
[59]X. Michalet and A. J. Berglund, "Optimal diffusion coefficient estimation in single-particle tracking," Phys. Rev. E **85**, 061916 (2012).
[60]W. Deng and E. Barkai, "Ergodic properties of fractional Brownian-Langevin motion," Phys. Rev. E **79**, 011112 (2009).
[61]H. Safdari, A. G. Cherstvy, A. V. Chechkin, F. Thiel, I. M. Sokolov, and R. Metzler, "Quantifying the non-ergodicity of scaled Brownian motion," J. Phys. A **48**, 375002 (2015).
[62]M. Schwarzl, A. Godec, and R. Metzler, "Quantifying non-ergodicity of anomalous diffusion with higher order moments," Sci. Rep. **7**, 3878 (2017).
[63]A. G. Cherstvy, S. Thapa, Y. Mardoukhi, A. V. Chechkin, and R. Metzler, "Time averaged and ergodic properties of the Ornstein-Uhlenbeck process: Particle starting distributions and relaxation to stationarity," Phys. Rev. E **98**, 022134 (2018).
[64]R. Hou, A. G. Cherstvy, R. Metzler, and T. Akimoto, "Biased continuous-time random walks for ordinary and equilibrium cases: Facilitation of diffusion, ergodicity breaking and ageing," Phys. Chem. Chem. Phys. **20**, 20827 (2018).
[65]A. G. Cherstvy, S. Thapa, C. E. Wagner, and R. Metzler, "Non-Gaussian, non-ergodic, and non-Fickian diffusion of tracers in mucin hydrogels," Soft Matter **15**, 2526 (2019).
[66]B. Bowers and E. D. Korn, "Cytochemical identification of phosphatase activity in the contractile vacuole of *Acanthamoeba castellanii*," J. Cell Biol. **59**, 784 (1973).
[67]N. Chenouard *et al.*, "Objective comparison of particle tracking methods," Nat. Methods **11**, 281 (2014).
[68]C. E. Wagner, "Micro- and macro-rheological studies of the structure and association dynamics of biopolymer gels," Ph.D. thesis, Massachusetts Institute of Technology, 2018.
[69]This can be an artifact of the tracking procedure and the limited resolution of the image-acquisition setup; see also Sec. V A.
[70]R. Motohashi and I. Hanasaki, "Characterization of aqueous cellulose nanofiber dispersions from microscopy movie data of Brownian particles by trajectory analysis," Nanoscale Adv. **1**, 421 (2019).
[71]E. Yamamoto, T. Akimoto, A. C. Kalli, K. Yasuoka, and M. S. P. Sansom, "Dynamic interactions between a membrane binding protein and lipids induce fluctuating diffusivity," Sci. Adv. **3**, e1601871 (2017).
[72]C. L. Vestergaard, P. C. Blainey, and H. Flyvbjerg, "Optimal estimation of diffusion coefficients from single-particle trajectories," Phys. Rev. E **89**, 022726 (2014).
[73]A. A. Sadoon and Y. Wang, "Anomalous, non-Gaussian, viscoelastic, and age-dependent dynamics of histonelike nucleoid-structuring proteins in live *Escherichia coli*," Phys. Rev. E **98**, 042411 (2018).
[74]A. G. Cherstvy, A. V. Chechkin, and R. Metzler, "Anomalous diffusion and ergodicity breaking in heterogeneous diffusion processes," New J. Phys. **15**, 083039 (2013).
[75]A. G. Cherstvy and R. Metzler, "Population splitting, trapping, and non-ergodicity in heterogeneous diffusion processes," Phys. Chem. Chem. Phys. **15**, 20220 (2013).
[76]T. Miyaguchi, T. Akimoto, and E. Yamamoto, "Langevin equation with fluctuating diffusivity: A two-state model," Phys. Rev. E **94**, 012109 (2016).
[77]S. Thapa, J. Krog, M. A. Lomholt, A. G. Cherstvy, and R. Metzler, "Bayesian model-comparison recipe for single-particle tracking data: Stochastic-diffusivity and fractional Brownian motion models," Phys. Chem. Chem. Phys. **20**, 29018 (2018).
[78]D. S. Martin, M. B. Forstner, and J. A. Käs, "Apparent subdiffusion inherent to single particle tracking," Biophys. J. **83**, 2109 (2002).
[79]A. J. Berglund, "Statistics of camera-based single-particle tracking," Phys. Rev. E **82**, 011917 (2010).
[80]K. Burnecki, E. Kepten, Y. Garini, G. Sikora, and A. Weron, "Estimating the anomalous diffusion exponent for single particle tracking data with measurement errors—An alternative approach," Sci. Rep. **5**, 11306 (2015).
[81]E. Kepten, A. Weron, G. Sikora, K. Burnecki, and Y. Garini, "Guidelines for the fitting of anomalous diffusion mean square displacement graphs from single particle tracking experiments," PLoS ONE **10**, e0117722 (2015).
[82]H. Qian, M. P. Sheetz, and E. L. Elson, "Single particle tracking. Analysis of diffusion and flow in two-dimensional systems," Biophys. J. **60**, 910 (1991).
[83]S. K. Ghosh, A. G. Cherstvy, and R. Metzler, "Non-universal tracer diffusion in crowded media of non-inert obstacles," Phys. Chem. Chem. Phys. **17**, 1847 (2015).
[84]A. G. Cherstvy, A. V. Chechkin, and R. Metzler, "Particle invasion, survival, and non-ergodicity in 2D diffusion processes with space-dependent diffusivity," Soft Matter **10**, 1591 (2014).
[85]S. K. Ghosh, A. G. Cherstvy, D. S. Grebenkov, and R. Metzler, "Anomalous, non-Gaussian tracer diffusion in crowded two-dimensional environments," New J. Phys. **18**, 013027 (2016).
[86]G. E. Uhlenbeck and L. S. Ornstein, "On the theory of the Brownian motion," Phys. Rev. **36**, 823 (1930).
[87]Y. Lanoiselee and D. S. Grebenkov, "A model of non-Gaussian diffusion in heterogeneous media," J. Phys. A: Math. Theor. **51**, 145602 (2018).
[88]M. V. Chubynsky and G. W. Slater, "Diffusing diffusivity: A model for anomalous, yet Brownian, diffusion," Phys. Rev. Lett. **113**, 098302 (2014).

[89]A. G. Cherstvy and R. Metzler, "Anomalous diffusion in time-fluctuating non-stationary diffusivity landscapes," Phys. Chem. Chem. Phys. **18**, 23840 (2016).
[90]A. V. Chechkin, F. Seno, R. Metzler, and I. M. Sokolov, "Brownian yet non-Gaussian diffusion: From superstatistics to subordination of diffusing diffusivities," Phys. Rev. X **7**, 021002 (2017).
[91]R. Jain and K. L. Sebastian, "Lévy flight with absorption: A model for diffusing diffusivity with long tails," Phys. Rev. E **95**, 032135 (2017).
[92]L. Luo and M. Yi, "Non-Gaussian diffusion in static disordered media," Phys. Rev. E **97**, 042122 (2018).
[93]V. Sposini, A. V. Chechkin, F. Seno, G. Pagnini, and R. Metzler, "Random diffusivity from stochastic equations: Comparison of two models for Brownian yet non-Gaussian diffusion," New J. Phys. **20**, 043044 (2018).
[94]V. Sposini, A. V. Chechkin, and R. Metzler, "First passage statistics for diffusing diffusivity," J. Phys. A: Math. Theor. **52**, 04LT01 (2019).
[95]Y. Golan and E. Sherman, "Resolving mixed mechanisms of protein subdiffusion at the T cell plasma membrane," Nat. Commun. **8**, 15851 (2017).
[96]A. G. Cherstvy *et al.* (unpublished).
[97]S. Yu, J. Sheats, P. Cicuta, B. Sclavi, M. Cosentino Lagomarsino, and K. D. Dorfman, "Subdiffusion of loci and cytoplasmic particles are different in compressed Escherichia coli cells," Nat. Commun. Biol. **1**, 176 (2018).
[98]F. Kindermann *et al.*, "Nonergodic diffusion of single atoms in a periodic potential," Nat. Phys. **13**, 137 (2017).
[99]C. Mark, C. Metzner, L. Lautscham, P. L. Strissel, R. Strick, and B. Fabry, "Bayesian model selection for complex dynamic systems," Nat. Commun. **9**, 1803 (2018).
[100]J.-H. Jeon, H. M.-S. Monne, M. Javanainen, and R. Metzler, "Anomalous diffusion of phospholipids and cholesterols in a lipid bilayer and its origins," Phys. Rev. Lett. **109**, 188103 (2012).
[101]Y. Lanoiselee,"Revealing the transport mechanisms from a single trajectory in living cells," Ph.D. thesis, Université Paris-Saclay, 2019.
[102]C. Mark, "Heterogeneous stochastic processes in complex dynamic systems," Ph.D. thesis, Friedrich-Alexander-Universität Erlangen-Nürnberg, 2018.
[103]M. el Beheiry, M. Dahan, and J.-B. Masson, "InferenceMAP: Mapping of single-molecule dynamics with Bayesian inference," Nat. Methods **12**, 594 (2015).
[104]A. Lee, K. Tsekouras, C. Calderon, C. Bustamante, and S. Presse, "Unraveling the thousand word picture: An introduction to super-resolution data analysis," Chem. Rev. **117**, 7276 (2017).
[105]C. Beck and E. G. D. Cohen, "Superstatistics," Physica A **322**, 267 (2003).
[106]C. Beck, "Superstatistical Brownian motion," Prog. Theor. Phys. Suppl. **162**, 29 (2006).
[107]S. Hapca, J. W. Crawford, and I. M. Young, "Anomalous diffusion of heterogeneous populations characterized by normal diffusion at the individual level," J. R. Soc. Interface **6**, 111 (2009).
[108]C. Metzner, C. Mark, J. Steinwachs, L. Lautscham, F. Stadler, and B. Fabry, "Superstatistical analysis and modelling of heterogeneous random walks," Nat. Commun. **6**, 7516 (2015).
[109]X. Wang, W. Deng, and Y. Chen, "Ergodic properties of heterogeneous diffusion processes in a potential well," e-print arXiv:1901.10857.
[110]J. Kärger, "NMR self-diffusion studies in heterogeneous systems," Adv. Colloid Interface Sci. **23**, 129 (1985).
[111]E. Fieremans, D. S. Novikov, J. H. Jensen, and J. A. Helpern, "Monte Carlo study of a two-compartment exchange model of diffusion," NMR Biomed. **23**, 711 (2010).
[112]T. C. Rösch, L. M. Oviedo-Bocanegra, G. Fritz, and P. L. Graumann, "SMTracker: A tool for quantitative analysis, exploration and visualization of single-molecule tracking data reveals highly dynamic binding of B. Subtilis global repressor AbrB throughout the genome," Sci. Rep. **8**, 15747 (2018).
[113]A. B. Kolomeisky, "Physics of protein-DNA interactions: Mechanisms of facilitated target search," Phys. Chem. Chem. Phys. **13**, 2095 (2011).
[114]A. G. Cherstvy, A. B. Kolomeisky, and A. A. Kornyshev, "Protein-DNA interactions: Reaching and recognizing the targets," J. Phys. Chem. B **112**, 4741 (2008).
[115]M. Bauer and R. Metzler, "Generalized facilitated diffusion model for DNA-binding proteins with search and recognition states," Biophys. J. **102**, 2321 (2012).
[116]T. Wagner, A. Kroll, C. R. Haramagatti, H.-G. Lipinski, and M. Wiemann, "Classification and segmentation of nanoparticle diffusion trajectories in cellular micro environments," PLoS ONE **12**, e0170165 (2017).
[117]A. C. H. Tsang, A. T. Lam, and I. H. Riedel-Kruse, "Polygonal motion and adaptable phototaxis via flagellar beat switching in the microswimmer *Euglena gracilis*," Nat. Phys. **14**, 1216 (2018).
[118]J. Mo and M. G. Raizen, "Highly resolved Brownian motion in space and in time," Ann. Rev. Fluid Mech. **51**, 403 (2019).
[119]Note that myosin-IC motors are abundant in the actin-rich edge of the cell, while myosin-II motors are present in the entire cytoplasm.
[120]Note that in this setup smaller vacuoles were technically harder to track because our detection algorithm is based on edge detection and subsequent Hough transformation, commonly used to detect circles. This procedure requires a threshold value for the minimal circle radius and for the sensitivity to be preset. So, if the radius is chosen too small, many "circles" that are not vacuoles would be undesirably detected.
[121]Note that the evaluation of the vacuoles' center-of-mass position[20] from their center-of-area coordinate requires an assumption of a *uniform cell height*. This has certain approximations. Fast-running AC cells appear to have a "fried-egg" geometry[13,16] with a *varying cell height* from the surface. The videos indicate that the cells have thin leading edge in front and rather thick "sack of material" on the rear end, where large vacuoles are often located; see the video files in the supplementary material.
[122]This hampers the detection of small vacuoles for longer times. During amoebae diffusion, larger particles stay in a confident-detection plane for longer times introducing certain bias in the data (see the discussion in Refs. 56, 65, 67, and 68). Specifically, the focus depth still allowing a confident tracking is a couple of μm. Larger vacuoles are, thus, allowed to move larger distances in the vertical direction and still yield a detectable position. By contrast, for smaller vacuoles, the same displacement may lead to its disappearance from the viewfield and to trajectory termination. Thus, a slower subpopulation of smaller vacuoles gets over-represented in the data set.
[123]Note that the discrepancy of the EB parameter from the Brownian behavior may seem inconsistent with a close match of the MSD and mean TAMSD, as seen in Fig. 16 in the Appendix. Theoretically, however, similar discrepancies in the behaviors of the ensemble- and time-averaged displacements versus the EB parameter were found and rationalized previously; see Ref. 76. This is the case, for instance, for diffusive systems where the relaxation time exceeds the measurement time (the length of time series).
[124]The TAMSD exponent varies substantially along the vacuole trajectories in the range of time-shifts probed for the autocorrelation function in Fig. 8. In virtue of a limited length of trajectories, the mean TAMSD does not reveal any *extended* region of anomalous diffusion with a roughly constant scaling exponent. Therefore, one cannot expect a universal curve for $C_{\delta t}(t)$ to emerge when a rescaling of time $t/\delta t$ is employed; see also the discussion in Ref. 52.
[125]This value, however, has a large standard deviation, again due to the fact that instantaneous speeds of vacuoles take rather discretized values in the current data set. Note here that small vacuoles which are slow can be over-represented in the current data set (generally, smaller tracers are more problematic to track for longer times; Fig. 14 in the Appendix confirms this statement).
[126]We emphasize here, however, that if the mean vacuole radii—rather than the maximum radii—are used for the analysis, the vacuole distributions appear quite different; see Fig. 21 in the Appendix. In this interpretation, for instance, the smallest vacuoles tend to occupy the central regions of the amoebae. The physical interpretation for the mean vacuole radius seems, however, less clear to us than for the maximum radius along a given track.
[127]To cure these "artificial" discreteness-based effects[69] in displacements, speeds, and displacement autocorrelations of vacuoles, one can think of *smearing out* the vacuole positions recorded in these SPT experiments, prior to their statistical analysis. One can use a Gaussian-like smoothening function with width equal to several pixels of the microscopy image [not shown; see the inset of Fig. 7(b)].

This would then make the peaks in the speed distribution of Fig. 9 originating from the discreteness effects less pronounced. The elementary time scale involved in the computation of the average vacuole speed should then also be adjusted correspondingly (instead of setting it to one elementary time step, as in Fig. 9); see Ref. 52. Physically, only those tracer displacements exceeding the position-localization uncertainty[52,58,78] should be used in the analysis of physical observables. The effects of varying localization error in these SPT experiments on the behavior of the fundamental quantities such as the TAMSD, the EB parameter, and the autocorrelation function would be interesting to study in the future[96] once precision-controlled data are acquired for this motile system.

[128]Possible *long-distance correlations* in direction and motion speed of diffusing vacuoles—as a function of their separation inside a given amoeba—are an interesting subject to study. They could quantify the "reach" of hydrodynamic and other correlation-inducing interactions being transmitted through the cell cytoplasm. In the current data, however, the mutual distances between vacuoles were not recorded and this question cannot be addressed in principle.